2022

Contamination of Finescale Strain Estimates of Turbulent Kinetic Energy Dissipation by Frontal Physics

Laur Ferris
Virginia Institute of Marine Science

Donglai Gong
Virginia Institute of Marine Science

Sophia Merrifield

Louis St. Laurent

Recommended Citation

Ferris, Laur; Gong, Donglai; Merrifield, Sophia; and St. Laurent, Louis, Contamination of Finescale Strain Estimates of Turbulent Kinetic Energy Dissipation by Frontal Physics (2022). *Journal of Atmospheric and Oceanic Technology*, 39(5), 609-640.
doi: 10.1175/JTECH-D-21-0088.1

Contamination of Finescale Strain Estimates of Turbulent Kinetic Energy Dissipation by Frontal Physics

LAUR FERRIS,[a,c] DONGLAI GONG,[a] SOPHIA MERRIFIELD,[b] AND LOUIS ST. LAURENT[c]

[a] *Department of Physical Sciences, Virginia Institute of Marine Science, William and Mary, Gloucester Point, Virginia*
[b] *Marine Physical Laboratory, Scripps Institution of Oceanography, University of California, San Diego, La Jolla, California*
[c] *Environmental and Information Systems, Applied Physics Laboratory, University of Washington, Seattle, Washington*

(Manuscript received 25 June 2021, in final form 20 December 2021)

ABSTRACT: Finescale strain parameterization (FSP) of turbulent kinetic energy dissipation rate has become a widely used method for observing ocean mixing, solving a coverage problem where direct turbulence measurements are absent but CTD profiles are available. This method can offer significant value, but there are limitations in its broad application to the global ocean. FSP often fails to produce reliable results in frontal zones where temperature–salinity (T/S) intrusive features contaminate the CTD strain spectrum, as well as where the aspect ratio of the internal wave spectrum is known to vary greatly with depth, as frequently occurs in the Southern Ocean. In this study we use direct turbulence measurements from Diapycnal and Isopycnal Mixing Experiment in the Southern Ocean (DIMES) and glider microstructure measurements from Autonomous Sampling of Southern Ocean Mixing (AUSSOM) to show that FSP can have large biases (compared to direct turbulence measurement) below the mixed layer when physics associated with T/S fronts are meaningfully present. We propose that the FSP methodology be modified to 1) include a density ratio (R_ρ)-based data exclusion rule to avoid contamination by double diffusive instabilities in frontal zones such as the Antarctic Circumpolar Current, the Gulf Stream, and the Kuroshio, and 2) conduct (or leverage available) microstructure measurements of the depth-varying shear-to-strain ratio $R_\omega(z)$ prior to performing FSP in each dynamically unique region of the global ocean.

SIGNIFICANCE STATEMENT: Internal waves travel through the ocean and collide, turbulently mixing the interior ocean and homogenizing its waters. In the absence of actual turbulence measurements, oceanographers count the ripples associated with these internal waves and use them estimate the amount of turbulence that will transpire from their collisions. In this paper we show that the ripples in temperature and salinity that naturally occur at sharp fronts masquerade as internal waves and trick oceanographers into thinking there is up to 100 000 000 times more turbulence than there actually is in these frontal regions.

KEYWORDS: Instability; Turbulence; Waves, oceanic; Fronts

1. Introduction

Mesoscale processes, submesoscale processes, and turbulent mixing within the Southern Ocean play critical roles in global ocean circulation. As a major component of global overturning circulation, North Atlantic Deep Water (NADW) upwells in the Southern Ocean. Much of this is modified to become Antarctic Bottom Water while the remaining NADW diverges northward to feed the upper cell of the Atlantic meridional overturning circulation (Talley 2013). While this paradigm of quasi-adiabatic upwelling is generally supported by numerical models (Thompson 2008), models do not capture realistic mixing physics. The role of ocean interior mixing, and relative importance of isopycnal versus diapycnal upwelling in Southern Ocean dynamics, is poorly understood (Waterhouse et al. 2014; Tamsitt et al. 2017). We are just beginning to understand the spatial and temporal inhomogeneity of upper ocean mixing in the Southern Ocean (Ferris et al. 2021, manuscript submitted to *J. Phys. Oceanogr.*). Vertical structure of eddy diffusivity in relation to water mass distribution determines where diapycnal mixing and upwelling/downwelling occurs. With the paucity of turbulent kinetic energy (TKE) dissipation measurements, it is tempting to widely apply finescale strain parameterization (FSP) as a substitute to extract turbulence information from plentiful CTD measurements in order to study global ocean mixing.

The processes driving mixing in the Southern Ocean are numerous. Below the surface mixed layer, these processes include double diffusive convection and interleaving/layering, shear-driven instabilities, internal wave–eddy interactions, and internal wave–wave interactions. The last is most central to downscale energy transfer. The process of forward energy cascade moves energy from the mainly geostrophic mesoscale (10 to 100 km), to the submesoscale (10 m to 10 km), consisting of nonlinear flows and internal waves, and down to the microscale (1 cm to 1 m) (St. Laurent et al. 2012; Sheen et al. 2015). While details of downscale energy transfer are active areas of research, it is accepted that forward energy cascade in the interior ocean is principally accomplished through internal wave–wave interactions. Triads of internal waves with summatively resonant wavenumbers and frequencies (Hasselmann's theorem) interact with each other [presumably

Denotes content that is immediately available upon publication as open access.

Corresponding author: Laur Ferris, lferris@apl.washington.edu

DOI: 10.1175/JTECH-D-21-0088.1

in the universal manner of the Garrett–Munk (GM) spectrum] until they break and release their energy as turbulent dissipation. TKE may dissipate locally at the site of internal wave generation via wave breaking, or internal waves may propagate energy away and dissipate at continental margins (Waterhouse et al. 2014).

The oceanic finescale consists of features that exist on vertical scales from 1–10 m to 100–1000 m. The Ozmidov scale, $L_{oz} = \varepsilon^{1/2}/N^{3/2}$ (~1 m), delineates finescale adiabatic processes (i.e., internal waves) from microscale diabatic, dissipative processes and describes the largest eddies that can overturn in a stably stratified water column. Numerous finescale parameterizations leverage CTD and/or velocity profiles to estimate TKE dissipation rate (ε), including Thorpe scales (Gargett and Garner 2008), shear- and/or strain-based finescale parameterizations (Polzin et al. 1995), and newer techniques such as the large-eddy method (Beaird et al. 2012); all rely on measurement of finescale features and the assumption that energy at the finescale dissipates at the microscale.

Thorpe scale analysis consists of algorithmically sorting fluid elements from a measured density profile into a stably stratified profile, while keeping track of required vertical displacements (Thorpe 1977). A Thorpe length scale (L_T) is obtained from the root-mean-square of tracked displacements. The value of ε is inferred from the assumed linear relationship $L_T \sim L_{oz}$. Dillon (1982) adopted the method for oceanic application (assuming temperature dominated the density in surface layers and seasonal thermoclines), with additional groups (Alford and Pinkel 2000) applying the same temperature-only method to depth-restricted regions where temperature alone was indicative of density overturns. Gargett and Garner (2008) extended the method to density overturns measured by wire-lowered CTD. Mater et al. (2015) with Scotti (2015) demonstrated clear bias (due to L_T/L_{oz} increasing with overturn size) in the Thorpe scale method using Vertical Microstructure Profiler (VMP) observations, though the method remains common.

Shear- and/or strain-based finescale parameterizations leverage the wave-driven forward energy cascade to estimate TKE dissipation rate (ε). The parameterization of mixing associated with internal wave interactions consists of assuming energy budget $P \cong -\rho\varepsilon + B$, such that turbulent production (P) is matched by ε and buoyancy flux (B). This spectral energy transfer occurs in a cascade of increasing wavenumbers (nonlinear wave motions of decreasing size), which is quantitatively estimated from CTD and/or ADCP measurements (Polzin et al. 2014). Gregg (1989) first developed the shear-based finescale parameterization. Observations used to characterize the oceanic shear and strain spectra in relation to microstructure measurements (Gregg and Kunze 1991) led to the development of the shear and strain-based method by Polzin et al. (1995), with generalization of the Gregg–Henyey parameterization to different latitudes using measurements of velocity and density via High Resolution Profiler (HRP). Kunze et al. (2006) offers a comprehensive discussion of applying Polzin et al.'s (1995) shear and strain-based method to lower-frequency (e.g., 50-m) LADCP data. Mauritzen et al. (2002) then introduced the method of strain-only finescale parameterization to study the Mid-Atlantic Ridge. Whalen et al. (2012, 2015) are known for the application of strain-only finescale parameterization to the Argo float array. There are numerous variations of the above parameterization such as that modified for use on the continental shelf (MacKinnon and Gregg 2003).

Finescale parameterizations based on shear and/or strain variances assume turbulent mixing in the ocean is primarily driven by internal wave–wave interactions (elastic scattering, induced diffusion, parametric instability) characterized by the GM model spectrum in the ocean. The GM model is an empirical representation of the canonical internal wave spectrum based on data collected from many regions of the ocean [see reviews by Munk (1981) and Gregg and Kunze (1991)]. The empirically derived parameters in the GM model represent numerous elements of spectral cascade physics, including energy transfers due to wave–wave, wave–eddy, and eddy–eddy interactions at scales larger than viscous dissipation. These interactions have been studied in stratified turbulence literature: direct numerical simulations (DNS)-based inquires have supported a highly anisotropic forward energy cascade in the inertial subrange characterized by wave features in the vertical and formation of layers in the horizontal, such that energy transfer from horizontal to vertical modes is a universal feature (Lindborg 2006; Kimura and Herring 2012). Velocity structure functions reveal the vortical and wave-attributable spectra to have distinct transition wavenumbers from 2D turbulence to 3D turbulence, complicating structure of energy spectra (Kimura and Herring 2012). Stratification is also shown to enhance nonlocal energy transfer between large and small horizontal scales (Khani and Waite 2013). Nevertheless, extremely fine numerical grids are required to confirm the spectra behavior observed in many of these studies (Bartello and Tobias 2013), leaving us to the continued observation of oceanic forward energy cascade. As such, the variation in stratification (N^2) or "strain spectra" is attributed to an internal wave field described by the GM spectrum and its associated energetics. This is a precarious assumption for the Southern Ocean (Kunze et al. 2006; Frants et al. 2013; St. Laurent et al. 2012; Sheen et al. 2013) as observations have shown that finescale parameterization techniques routinely overestimate ε even when a conservative shear-to-strain ratio (R_ω) is assumed (Merrifield 2016). The best agreement is thought to be in the ocean interior where the assumed dominance of wave–wave interactions likely holds. The presence of fronts and eddies can further modify the observed shear and strain to deviate from the presumed GM spectrum.

Adopting the methodology of Whalen et al. (2012) and Huussen et al. (2012) the FSP of ε is given by Eq. (1):

$$\varepsilon_{\text{strain}} = \varepsilon_0 \frac{\overline{N^2}}{N_0^2} \frac{\left\langle \xi_z^2 \right\rangle^2}{\left\langle \xi_{z\text{GM}}^2 \right\rangle^2} h(R_\omega) L(f, N), \tag{1}$$

$\left\langle \xi_z^2 \right\rangle$ is the strain variance determined by integrating the strain spectra, leveraging the property that area under a one-sided

power spectrum is equal to its variance; $L(f, N)$ is a latitudinal correction for the oceanic internal wavefield's frequency content; and $h(R_\omega)$ is the dependence on the internal wavefield's shear-to-strain ratio R_ω (Kunze et al. 2006; Polzin et al. 1995), which must be assumed in the absence of shear, typically $R_\omega \sim 3$.

Recently strain-only finescale parameterization has been used to infer climatological patterns of global mixing from WOCE/CLIVAR lowered CTD (Huussen et al. 2012) as well as Argo profiling floats (Whalen et al. 2015). In the latter case this technique is uniformly applied to the global ocean including the frontal zones such as the Drake Passage of the Antarctic Circumpolar Current (ACC), Gulf Stream, and Kuroshio. These studies produce turbulent dissipation estimates in a climatological rather than time-varying sense. Frants et al. (2013) performed FSP and Thorpe scale analysis on Diapycnal and Isopycnal Mixing Experiment in the Southern Ocean (DIMES) CTD but did not examine how their efficacy changes in intense frontal zones. These methods have yet to be widely adopted for use by glider platforms, but Johnston and Rudnick (2015) applied the strain-only finescale parameterization to glider data, with agreement between shear-and-strain and strain-only estimates of diffusivity within a factor of 1.7. An important consideration is that gliders, contrary to free-falling vertical profilers, sample at an angle. Whereas Thorpe scales depend on careful measurement of the vertical organization of water parcels and could underestimate turbulent dissipation rates associated with high-aspect-ratio Kelvin–Helmholtz billows or through observation of false overturns (Thorpe 2012), FSP leverages the assumed isotropy of a somewhat universal wavenumber spectra and is more robust to glider usage.

We examine key assumptions of FSP, which overall assumes that energy in the internal wavefield smoothly transitions to turbulent dissipation. By measuring both the internal wave scale (using FSP) and the microscale we can assess this paradigm. Strain is defined as the distance between two isopycnal surfaces divided by their mean separation (Thorpe 2005). There are three assumptions underlaying the application of FSP in the real ocean. Assumption 1 is that observed strain-like features are indeed internal wave strain. Assumption 2 is that the shear-to-strain ratio in the ocean is similar to the GM spectrum such that its value R_ω may be assumed. Assumption 3 is that downscale energy transfer is driven by nonlinear interactions between internal waves (Polzin et al. 2014) such that for a control volume, production of TKE by shear matches the dissipation by molecular viscosity and buoyancy flux—ignoring the divergence, pressure work, and transport terms of the TKE equation.

Assumption 1 implies variations in observed buoyancy frequency (N^2) result from internal wave strain acting on the density field. Double diffusive instabilities (endemic to Southern Ocean and other intense frontal regions) could contaminate the strain spectrum via temperature–salinity (T/S) intrusive features. A feature of the ACC is numerous named fronts, water mass boundaries where collections of filaments demarcate abrupt changes in T/S relation. The Subantarctic Front (SAF) is the northern edge of the ACC and divides Upper Circumpolar Deep Water from Subantarctic Mode Water (SAMW) which overlies low-salinity Antarctic Intermediate Water. Further south the Polar Front (PF) is demarcated by abrupt changes in sea surface temperature and the subduction of Antarctic Surface Water beneath SAMW. Outcropping of isopycnals in this frontal system creates horizontal juxtapositions of water masses with contrasting T/S relationships, predisposing them to double diffusive instabilities. The PF region is predisposed to double diffusive instabilities (Schmitt 1994) because warm/salty subantarctic waters are to the north and cold/fresh Southern Ocean waters are to the south.

Double diffusive instabilities occur because thermal diffusivity is much greater than salt diffusivity ($\kappa_S \approx 1 \times 10^{-9}$ m^2 s^{-1}, $\kappa_T \approx 1.5 \times 10^{-7}$ m^2 s^{-1}). In its salt fingering regime (Schmitt 1994), warm/salty water overlies cold/freshwater, and a parcel displaced into the upper layer warms faster than it experiences a salinity change such that it becomes a warm/fresh particle and continues to rise. In its diffusive/oscillatory regime, cold/freshwater overlies warm/salty water, and a particle displaced upward conductively loses heat before sinking as lukewarm/salty water back to the initial position, subsequently overshooting its initial position (producing a growing oscillation). The oscillation forms its own well-mixed layer until the temperature gradient between the mixed layer and the adjacent water grows to become critically unstable and forms a convective layer. Double diffusive instabilities need not be vertical; horizontal double diffusive instabilities (interleaving, intrusive layering) ~10–100 m in scale are known to occur in the Drake Passage, contributing heavily to lateral mixing. Observationally, north of the PF and its vicinity have been shown to favor salt fingering, while south of the PF favors diffusive convection (Merrifield et al. 2016). A T/S-intrusive signal would manifest itself in FSP as the available potential energy (strain) spectra having an unusual rolloff at high wavenumbers (values would be too high). T/S-intrusive signals can be identified using the density ratio $R_\rho = \alpha T_z/\beta S_z$, useful for determining whether a profile is prone to the diffusive ($0.5 < R_\rho < 1$) or the salt fingering ($1 < R_\rho < 2$) regime. These ranges are those for which instability can develop faster than local buoyancy period $2\pi/N$ (Schmitt 1994).

Assumption 2 arises specifically for FSP (which lacks shear information). FSP assumes an idealized, universal GM spectrum; an empirically determined imagined-to-be universal function that describes the variation of wave energy in horizontal wavenumber, vertical wavenumber, and frequency space. By assuming a GM shear-to-strain ratio R_ω we presume GM shear characteristics in the internal wavefield and thus assume its frequency content. Internal wave–wave interactions smooth the shape of spectrum, making it redder; the GM spectrum is intended to apply far away from contamination by boundaries and specific internal waves sources such that internal waves have had sufficient time and space to collide and smooth the spectrum so there is no longer any prominence in wavenumber or frequency (Polzin and Lvov 2011). FSP could fail in the Southern Ocean because it does not necessarily meet this criterion due to prominent internal lee-wave generation.

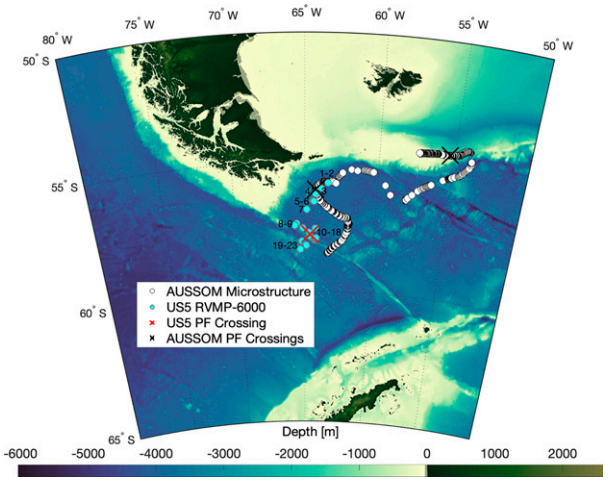

FIG. 1. Field data. Showing synchronous microstructure and CTD profiles from the DIMES US5 cruise (October–November 2013) and AUSSOM glider survey (November–December 2017) used for comparison of TKE dissipation rate estimated from finescale strain parameterization (FSP) to direct measurements. The Polar Front (PF) is a dynamic, meandering structure that changes location over time and marks the subduction of cold, fresh Southern Ocean water beneath warm, salty subantarctic water.

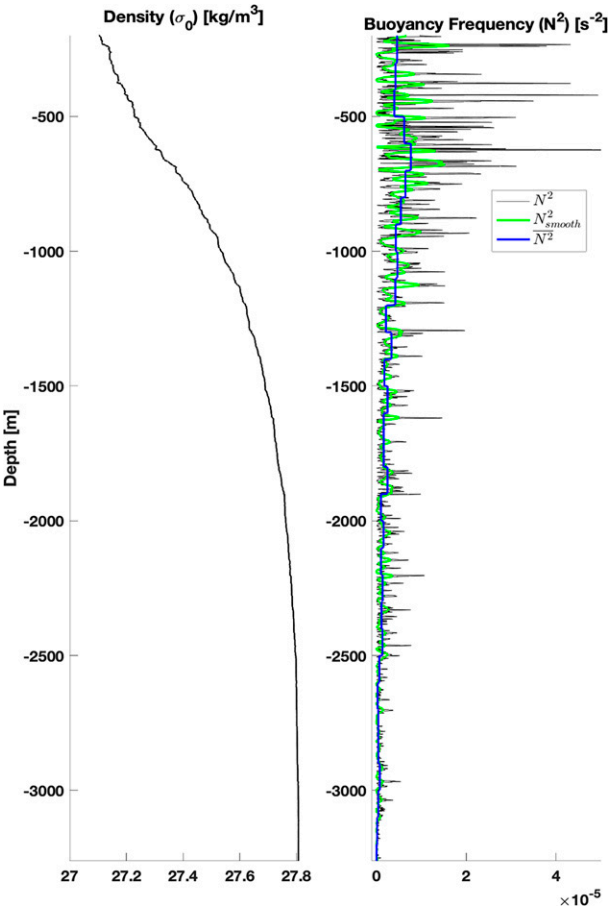

FIG. 2. Three forms of buoyancy frequency used in [Eq. (1)], calculated for DIMES US5 profile 17. To be clear, the density profile is not directly involved in the calculation of strain and is just provided for reference.

Due to weak stratification, large injection of kinetic energy, and the presence of continuous zonal jets, the Southern Ocean is highly influenced by topographic interaction in addition to geostrophic turbulence (Ferrari and Wunsch 2009). Deep flow (e.g., a mesoscale eddy, jet, barotropic tide) impinging on rough topography $h = h_0 \sin[k(x + Ut)]$ generates topographic lee waves with frequency $\omega = Uk$, where k is the horizontal wavenumber of the seafloor topographic feature and U is the horizontal flow velocity. (In reality the seafloor is a combination of features with different wavenumbers such that the lee wave spectra is a summation of Fourier modes.) Internal lee waves generated by flow–topography interactions appear to dissipate only a fraction of the total lee wave energy locally (Brearley et al. 2013); waves in the "hydrostatic nonrotating range" $U/N < k^{-1} < U/f$ can radiate upward, such that internal lee waves have an intrinsic frequency range of $f^2 < k^2U(z)^2 < N^2$ (Bell 1975). Lee waves are hypothesized to be more dominant in Southern Ocean than is ubiquitous in the global ocean (MacKinnon et al. 2017), and an internal wave spectrum with a prominent lee wave peak in wavenumber and frequency space is not a GM spectrum and implies a departure from the assumed $R_\omega = 3$. Furthermore R_ω is fixed for a single wave and is inherently a biased estimator of the full spectrum (Polzin et al. 1995, 2014).

If the true shear-to-strain ratio is higher (lower) than assumed R_ω in any part of the water column, ε_{FSP} will be an underestimate (overestimate) of true ε with an error directly proportional to R_ω. Internal waves at tidal frequency are associated with lower R_ω, while internal waves at near-inertial frequency are associated with higher R_ω. Chinn et al. (2016) find values ranging from 1 to 10; Waterman et al. (2013) report 7 over the Kerguelen Plateau, implying more energy in the near-inertial peak than the GM model spectrum. From studies of the Drake Passage and Scotia Sea (Fig. 16 from Kunze et al. 2006; Nikurashin and Ferrari 2010) $R_\omega = 10$ is appropriate. R_ω is effectively a ratio of horizontal kinetic to available potential energy. Near-inertial internal waves (having frequencies near f) are considered part of the *hydrostatic rotating wave regime* and have dominantly horizontal and rotational motions, while waves with frequencies near N are part of the *nonhydrostatic wave regime* and have predominately vertical motions (Gill 1982). This can be seen from the expression for lee wave vertical wavenumber $m^2/k^2 = (N^2 - \omega^2)/(\omega^2 - f^2)$. It follows that waves with frequencies near f (near N) have a high (low) shear-to-strain ratio. Nikurashin and Ferrari attribute this high $R_\omega = 10$ to inertial oscillations triggered by momentum flux divergence (caused by large-amplitude internal waves).

Assumption 3 is that energy feeding turbulent dissipation comes from nonlinear internal wave–wave interactions. FSP estimates the turbulent dissipation attributable to internal wave driven interactions, that is if internal waves predominately drive TKE injection into the microscale. If physical processes which can shortcut the steady forward energy

TABLE 1. Variables of finescale strain parameterization (FSP). Showing variables used in FSP [Eqs. (1)–(5)].

Variable	Unit	Description
$\varepsilon_{\text{strain}}$	W kg^{-1}	Estimated TKE dissipation rate [Eq. (1)]
ε_0	W kg^{-1}	6.63×10^{-10}, canonical GM dissipation rate for N_0 at latitude 30°
N_0	rad s^{-1}	5.24×10^{-3}, canonical GM buoyancy frequency
N	rad s^{-1}	Buoyancy frequency computed from CTD, e.g., via Gibbs SeaWater Oceanographic Toolbox
$\overline{N}$	rad s^{-1}	Mean buoyancy frequency for each segment, bin averaged from N
N_{smooth}	rad s^{-1}	Buoyancy frequency smoothed using quadratic fitting (Kunze et al. 2006) or calculated from CTD using adiabatic leveling (Huussen et al. 2012), e.g., via github.com/OceanMixingCommunity/Standard-Mixing-Routines. The latter is used here
$\langle \xi_z^2 \rangle$	—	Observed strain variance [Eq. (4)]
$\langle \xi_{z\text{GM}}^2 \rangle$	—	GM strain variance [Eq. (4)]
S_{str}	(rad m^{-1})$^{-1}$	Strain spectrum computed from ξ_z for each segment using Welch's power spectral density estimate (Welch 1967)
S_{strGM}	(rad m^{-1})$^{-1}$	GM model strain spectrum computed from f and $\overline{N}$ for each segment, e.g., via github.com/jklymak/GarrettMunkMatlab (Gregg and Kunze 1991) parameters are used here
$k_{\text{min}} = 2\pi/\lambda_{\text{max}}$	rad m^{-1}	Low-wavenumber integration limit, $2\pi/100$ m is used here. λ_{max} should not be larger than the segment length (i.e. the fundamental wavenumber), nor ~150 m to avoid accidental eddy contributions (Kunze et al. 2006)
$k_{\text{max}} = 2\pi/\lambda_{\text{min}}$	rad m^{-1}	High-wavenumber integration limit, $2\pi/10$ m is used here. This should be chosen to avoid the high-wavenumber rolloff, as well as be below the Nyquist wavenumber of sampling resolution Δz
L	—	Correction for latitudinal variability of internal wavefield [Eq. (5)]
f	rad s^{-1}	Coriolis frequency
f_{30}	rad s^{-1}	7.2921×10^{-5}, reference Coriolis frequency at latitude 30°
h	—	Dependence on shear-to-strain ratio [Eq. (3)], reduces to 1 when $R_\omega = 3$
R_ω	—	Shear-to-strain ratio, 3 assumes GM frequency spectrum but we use 10 after Kunze et al. (2006) and Nikurashin and Ferrari (2010)
ξ_z	—	Strain computed for each segment [Eq. (2)]
Δz	m	Sampling resolution within each segment, typically $\Delta z \approx 1$ m for DIMES US5 and $\Delta z \approx 0.3$ m for AUSSOM

cascade are active, FSP would be biased low (there is more energy dissipating at the microscale than contained by the internal wave field). Energetic shortcuts include surface forcing (wind shear and buoyancy flux), wave–flow interactions (critical layers), and frontal instabilities (e.g., parallel shear, centrifugal, inertial, baroclinic–symmetric). Observational studies of Southern Ocean mixing (e.g., SOFine and DIMES) have found enhanced TKE dissipation over regions of complex topography leads to generation of internal waves (Nikurashin et al. 2014; St Laurent et al. 2012; Waterman et al. 2013) suggesting that this system is sufficiently dominated by internal wave–wave interactions and this assumption (below the surface boundary layer) is likely truer than assumptions 1 and 2.

In the absence of microstructure coverage, FSP estimates of turbulence from lowered CTD and autonomous profiling floats are useful for our understanding of mixing in the global ocean; and the numerical models we construct from our understood reality. Acknowledging that core assumptions of FSP may be incompatible with frontal physics, it is important to reexamine the use of FSP in frontal zones. In this study we pair the wealth of microstructure data collected during DIMES with a first-of-its-kind glider survey (Fig. 1) to test FSP in an intense frontal zone—the Drake Passage and Scotia Sea regions of the Antarctic Circumpolar Current. Understanding FSP and its representation of downscale energy transfer in frontal regions is necessary for progressing TKE estimation from unmanned platforms, as well as understanding the global patterns of diapycnal diffusivity from which we understand ocean circulation and calibrate large-scale circulation models.

2. Methods

The Autonomous Sampling of Southern Ocean Mixing (AUSSOM) study was conducted in the Drake Passage region between the end of austral winter (November 2017) and the beginning of austral spring (February 2018). As part of this study, a Slocum glider *Starbuck* with a Rockland MicroRider microstructure sensor collected a 6-week turbulence record spanning 800 km from the Shackleton Fracture Zone to the Falkland Plateau. *Starbuck* was deployed on 16 November 2017 during LMG-1802 from the R/V *Laurence M. Gould*, sampled the PF for 60 days until sampling was disabled to preserve battery, and was recovered near Port Stanley, Falkland Islands, on 5 February 2018. The AUSSOM mission collected

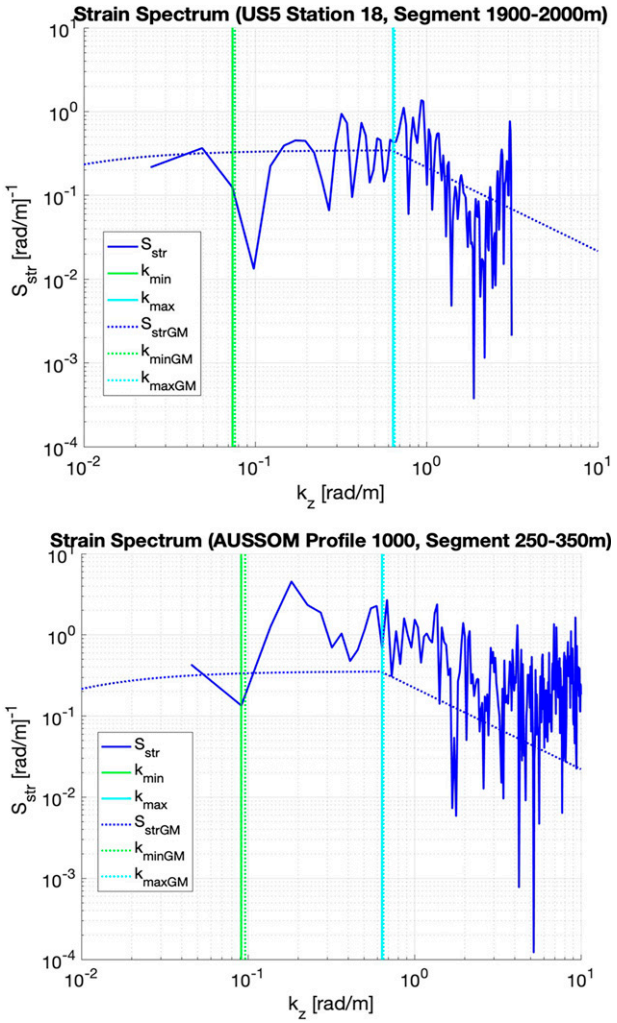

FIG. 3. Example strain spectra and limits of integration [Eq. (4)] for one segment of DIMES US5 and one segment of AUSSOM (corresponding to 0915 UTC 13 Dec 2017).

3028 CTD profiles and 932 microstructure profiles at depths 0–350 m. Details of glider-based microstructure are described in St. Laurent and Merrifield (2017). Ferris et al. (2021, manuscript submitted to *J. Phys. Oceanogr.*) previously used this dataset to quantify bias in boundary layer scalings of shear turbulence.

Cruise US5 (NBP1310A) was the Drake Passage leg of the DIMES and took place at the end of austral winter in 2013 (from 26 October through 13 November) on the RVIB *Nathaniel B. Palmer*. The cruise included 48 CTD and LADCP stations, with 23 full-depth microstructure profiles downstream of Phoenix Ridge and over the Shackleton Fracture Zone. Many of stations were around the SAF and PF. Full-depth microstructure was collected using a free-falling Rockland VMP-6000 with dual shear and thermistor probes. Cruise reports for all DIMES cruises are available at http://dimes.ucsd.edu. The DIMES US5 VMP-6000 and AUSSOM glider were each equipped with a SeaBird CTD (a pumped CTD in the case of the glider). Our analysis utilizes these two datasets and proceeds as follows: 1) For DIMES, we compute $\varepsilon_{\mathrm{FSP}}$ from CTD data collected at the 23 microstructure stations and compare it to directly measured ε from the VMP. 2) For AUSSOM, we compute $\varepsilon_{\mathrm{FSP}}$ from the glider CTD and compare it to measured ε from the Rockland microstructure sensor. 3) Calculate R_ρ for each of these CTD records to identify T/S-intrusive regions. 4) Examine the FSP bias $\log_{10}(\varepsilon_{\mathrm{FSP}}/\varepsilon)$ in fronts and T/S-intrusive regions.

We apply the FSP methodology as follows. First, we subdivide CTD profiles into vertical segments; we use half-overlapping 100-m segments and average the primary segments with secondary (staggered) segments to produce FSP estimates over 50-m intervals. For DIMES US5, segments span from 200 to 4200 m (or the VMP profile depth), eliminating shallow depths. For AUSSOM, segments span from 150 to 350 m. We are confident that this shallower choice is safe after analyzing actively mixing layer and mixed layer dynamics in Ferris et al. (2020, 2021, manuscript submitted to *J. Phys. Oceanogr.*); it is well below the mixed and actively mixing layers. The value of $\varepsilon_{\mathrm{FSP}}$ [Eq. (1)] is computed for each segment of each profile. Next we calculate the strain [Eq. (2)], which utilizes three forms of buoyancy frequency (Table 1) to quantify the density deformation of the water column:

$$\xi_z = \frac{N^2 - N^2_{\mathrm{smooth}}}{\overline{N^2}}, \tag{2}$$

which are demonstrated in Fig. 2. Fluid strain is similar to mechanical strain (a tensor metric of material deformation) [Eq. (2)], effectively quantifies the deformation in stratification, assumed to be caused by internal waves (IW). Equation (2), rather than the formal definition of fluid strain, is used because time-mean density profiles are unavailable; in their absence the segment scale is assumed to represent the time mean and variations within the segment scale represent IW activities (discussed in Mauritzen et al. 2002). By estimating the deformation, we estimate the internal wavefield and its energy content, and assume this energy at the finescale will dissipate as TKE at the microscale.

The connection between fluid deformation at the finescale and IW energy contained by that scale is the GM model spectrum, which is used as a reference to estimate IW energy from strain. The GM spectrum describes IW energy as a function of IW wavenumber (relatable to strain) and IW frequency (relatable to shear). In the absence of fluid velocity information, dependence on shear is calculated [Eq. (3)] from an assumed shear-to-strain ratio R_ω:

$$h(R_\omega) = \frac{1}{6\sqrt{2}} \frac{R_\omega(R_\omega + 1)}{\sqrt{R_\omega - 1}}, \tag{3}$$

and our focus is narrowed to comparing the observed strain to reference strain using the ratio of their variance $\langle \xi_z^2 \rangle / \langle \xi_{z\mathrm{GM}}^2 \rangle$. For a stationary ergodic random process, spatial-domain variance of a signal (strain in this case) is equal to its spectrum integrated over wavenumber in the wavenumber domain. It is advantageous to compute the variance of each strain segment in the wavenumber domain (rather than the spatial domain) to facilitate comparison with the GM spectrum (which is

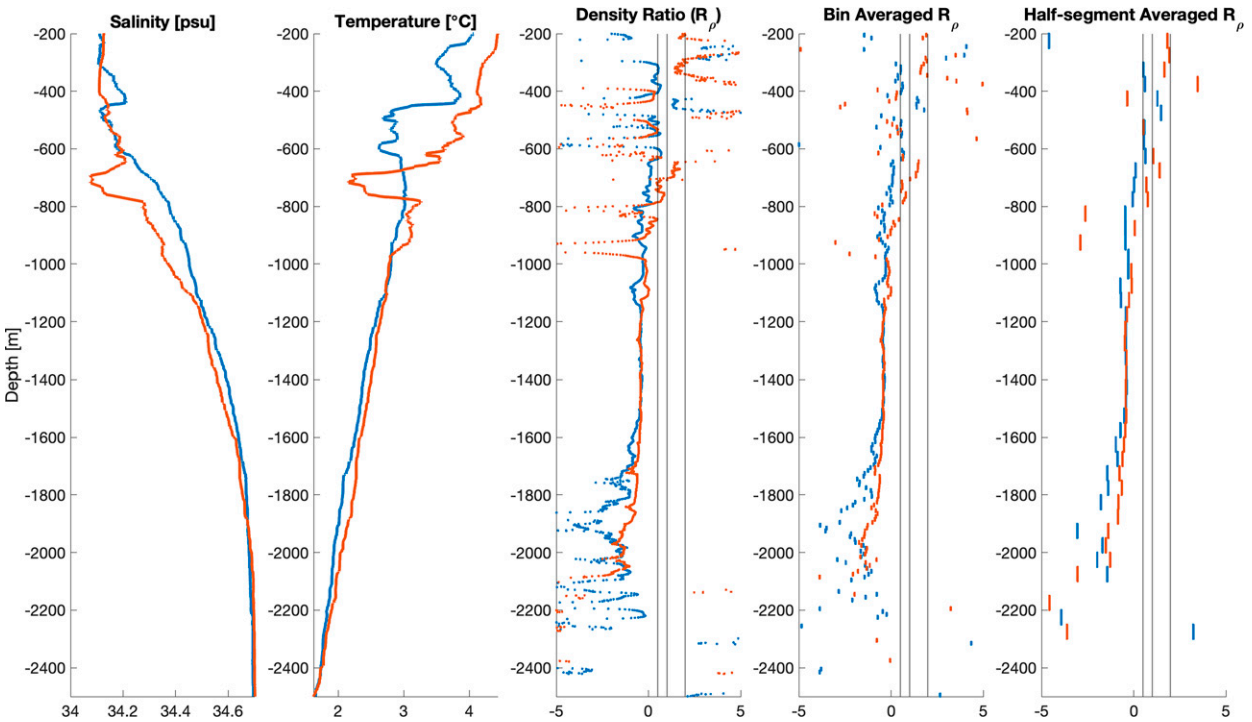

FIG. 4. Calculation of density ratio R_ρ for two profiles, stations 2 (blue) and 14 (orange), of US5. Values falling between vertical lines indicate stratification favorable to double diffusive instability.

function of wavenumber). Observed and GM strain variances $\left(\left\langle \xi_z^2 \right\rangle$ and $\left\langle \xi_{z\mathrm{GM}}^2 \right\rangle\right)$ are calculated from their respective spectra (S_{str} and S_{strGM}) over an identical range of wavenumbers (k) using [Eq. (4)] (Fig. 3):

$$\left\langle \xi_z^2 \right\rangle = \int_{k_{\min}}^{k_{\max}} S_{\mathrm{str}}(k)dk. \tag{4}$$

Prior to calculating the observed strain spectrum S_{str} each segment ξ_z is detrended, and a convolution window with 10% $\sin^2$ taper is applied in order to minimize spectral distortion of the segment's wavenumber content due to discontinuity at the edges. In other words, the first and last tenth of the segment are smoothly brought to zero using multiplicative factor $\sin^2[0.1(\pi z/2n)]$, where n is length of the strain segment. The spectrum S_{str} is corrected for power lost to windowing and multiplied by transfer function $\mathrm{sinc}^{-2}(k\Delta z/2\pi)$ to correct for finite differencing, where $\mathrm{sinc}(x) = \sin(\pi x)/(\pi x)$ and Δz is the vertical resolution of each segment.

Following concerns that at high energy levels the measured strain spectrum could become saturated (transition to 3D turbulence) before the high energy rolloff point k_c (Gargett 1990) such that Eq. (4) might erroneously include part of the dissipation scale and overestimate the strain variance, it has been popular to adjust the high wavenumber (low wavelength) integration limit until $\left\langle \xi_z^2 \right\rangle \leq 0.1$ or 0.2 (Huussen et al. 2012; Whalen et al. 2015). The practice evolved from the sensible usage of this integral constraint in Kunze et al. (2006), but we suggest reconsideration of this convention for two reasons. The first reason is that advances in sensing technology since 1990 have rendered the practice obsolete. We can measure strain to much smaller scale (1 m for DIMES US5 and ~0.3 m for AUSSOM, which are furthermore free-falling and uncontaminated by ship heave around the 10-m scale), have greater confidence that k_c seen in the spectrum is truly the rolloff point, and do not need to discard that much of the internal wave subrange (Klymak and Moum 2007). Our ability to select $k_{\max} \approx k_c$ makes this study robust to additional sources of bias such as wave–flow (critical layer) interactions which are problematic when $k_{\max} \ll k_c$ (Polzin et al. 2014; Waterman et al. 2013).

The second reason is purely logical. Deliberately constraining integration limits [Eq. (4)] beyond the observed rolloff point (to always produce a strain variance of $\left\langle \xi_z^2 \right\rangle \leq 0.1$) manipulates the observed strain variance $\left\langle \xi_z^2 \right\rangle$ until it matches what we desire. The spectrum is not necessarily parallel to GM spectrum; therefore, picking and choosing different subsets of the internal wave subrange to include in our strain variance calculation can produce wildly different strain variances; it is most accurate to use as much of the internal wave subrange as possible. There is no ontological reason for applying this criterion other than as a workaround for not being able to consistently determine k_c given measurement limitations (applicable when resolved strain was coarser). From inspection of S_{str} versus k, a choice of $k_{\max} = 2\pi/\lambda_{\min} = 10$ m is a suitable k_c for our datasets.

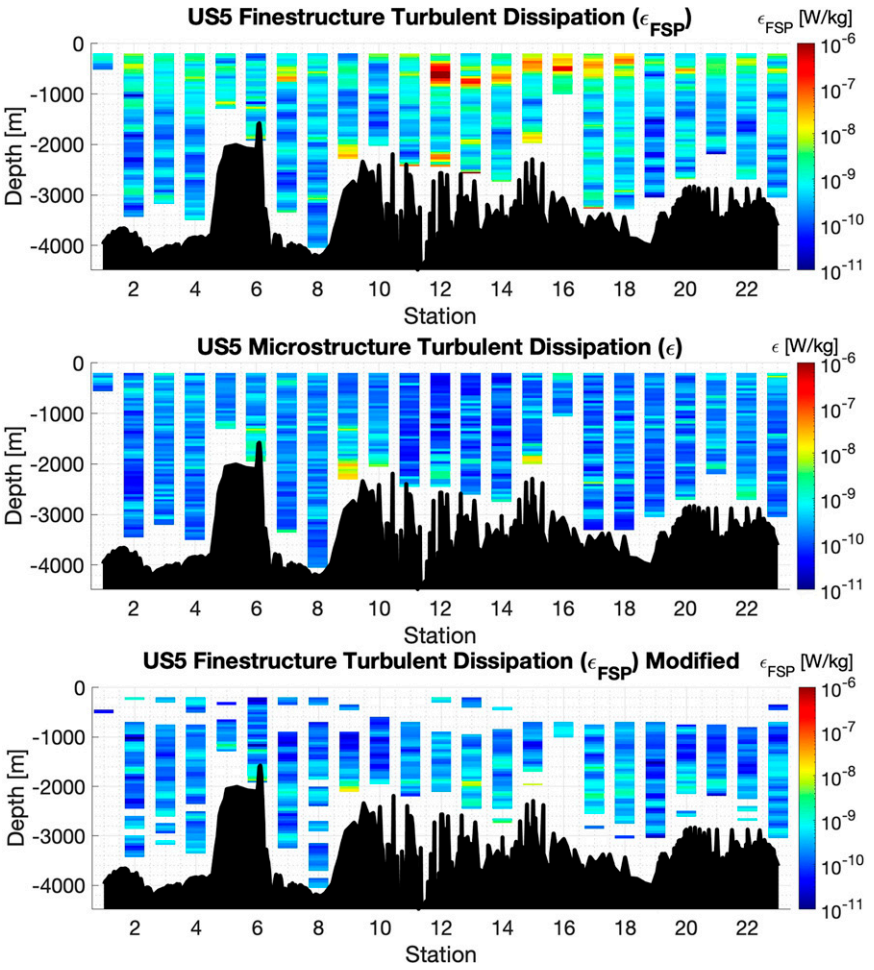

FIG. 5. (top),(middle) FSP-estimated and measured TKE dissipation rate for US5. Measured dissipation rate has been bin averaged to facilitate comparison with estimated dissipation. (bottom) Modified FSP (Fig. 11, discussed later) using a shear-to-strain ratio R_ω, which transitions from 3 to 10, as in Fig. 10. Additionally, all data prone to *T*/*S*-intrusive features have been removed from use.

A correction for latitudinal variability of internal wavefield is calculated [Eq. (5)] for each segment. All variables are summarized in Table 1:

$$L(f,N) = \Re\left\{\frac{f\cosh^{-1}(\overline{N}/f)}{f_{30}\cosh^{-1}(N_0/f_{30})}\right\}. \tag{5}$$

Shear- and/or strain-based finescale parameterizations do not apply to the continental shelf where the assumption of a broadband, source-agnostic IW wave spectrum fails outright (MacKinnon and Gregg 2003), and so we omit AUSSOM profiles beyond the continental rise. This leaves 1504 CTD profiles, 739 of which have synchronous microstructure. Due to the large spatial extent of the AUSSOM dataset and spatial variability of TKE dissipation rates in the Drake Passage and Scotia Sea, we elect not to average adjacent CTD profiles in order to investigate the success or failure of each individual application of FSP. Finally, before proceeding we wish to discuss a nuance of averaging that is often not mentioned in turbulence literature. Arithmetic means are commonly used to estimate the first probability moment (average) when data are normally distributed or close to it. TKE dissipation rate is not normally distributed as values often span multiple orders of magnitude (rather, it is log-skew-normally distributed; Cael and Mashayek 2021), such that the arithmetic mean is more like a maximum than an unbiased estimator of centroid. This issue of large values dominating the arithmetic mean is discussed in Waterman et al. (2013). Arithmetic means can be used to obtain average energetics from uniformly distributed TKE dissipation rates, but should not be used to evaluate biases in the statistical ensemble of turbulence parameterizations. As such, we apply logarithmic transformation before taking the mean, giving the better estimator [Eq. (6)]:

$$\hat{\varepsilon} = \frac{1}{n}\sum_{n=1}^{n}\log_{10}\varepsilon_n, \tag{6}$$

which is the geometric mean.

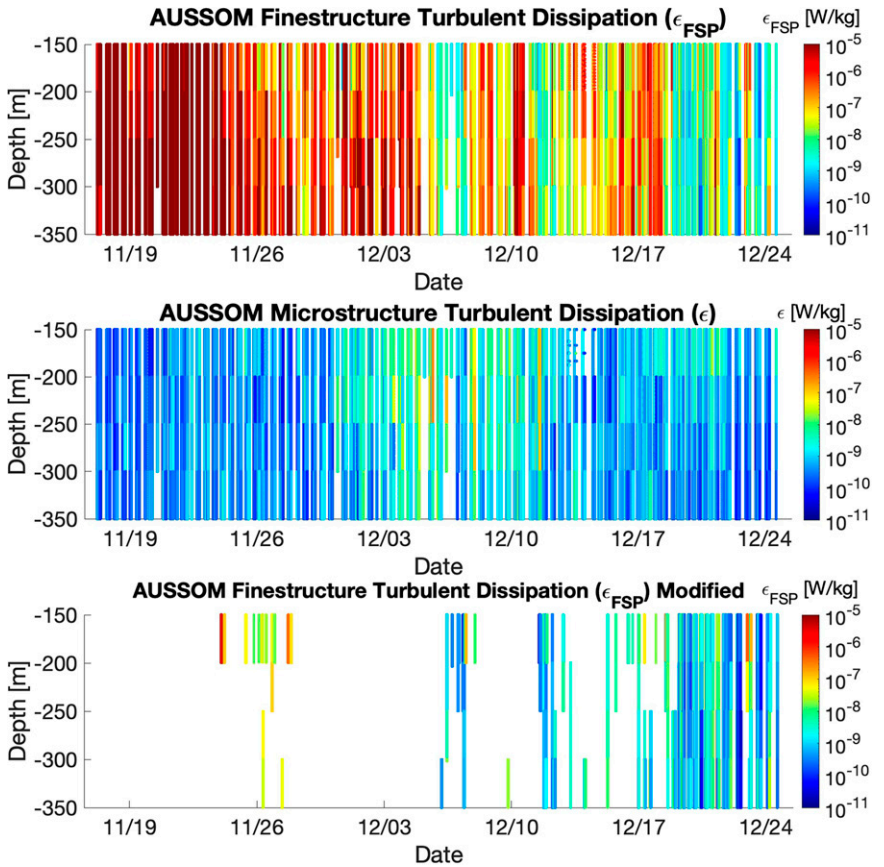

FIG. 6. (top),(middle) FSP-estimated and measured TKE dissipation rate for AUSSOM. Measured dissipation rate has been bin averaged to facilitate comparison with estimated dissipation. (bottom) Modified FSP (Fig. 11, discussed later) using a shear-to-strain ratio R_ω, which transitions from 3 to 10 as in Fig. 10. Additionally, all data prone to *T*/*S*-intrusive features have been removed from use.

To find density ratio R_ρ for each segment (Fig. 4), the procedure is to take a moving average of absolute salinity and conservative temperature with a window of approximately 33 meters. Then R_ρ is calculated using the Gibbs SeaWater (GSW) Oceanographic Toolbox of the International Thermodynamic Equation of Seawater—2010 (TEOS-10). For section plots (Figs. 7a, 8a, 13) R_ρ is averaged in 10-m vertical bins (chosen based on the expected scale of *T*/*S* intrusions) to facilitate visual comparison with TKE dissipation rate. For instances requiring a single representative value of $\overline{R_\rho}$ for each half segment (Figs. 7b, 8b, 15a), R_ρ is averaged in 50-m vertical bins. In both cases, the procedure is to first check for the presence of $0.5 < R_\rho < 2$ (indicative of double diffusive instability) within a bin; then take the average of doubly unstable values if present, or all values if no unstable R_ρ are found. In rare cases where multiple stable values ($R_\rho < 0.5$ or $2 < R_\rho$) average to produce a mean falsely indicative of stratification unstable to double diffusive instability, only R_ρ of the dominant side are averaged, e.g., $\overline{R_\rho} = (-100 + 51 + 52)/3 = 1$ would become $\overline{R_\rho} = (51 + 52)/2 = 51.5$. This scheme ensures the identification of bins containing subparts favorable to double diffusive instability when the entire segment is not doubly unstable. This method could create a discontinuity near $\overline{R_\rho} = 0.5 \cup 2$ in the x axis $\left(\overline{R_\rho}\right)$ but has no influence on the y axis (bias or magnitude of ε_{FSP}).

3. Results

For DIMES US5 (Fig. 5a) FSP estimates of TKE dissipation (ε_{FSP}) of show good agreement with microstructure measurements (ε) below the main thermocline. FSP captures but underestimates bottom-intensified ε at stations 6, 9, 12, and 15 as expected; the GM spectrum does not represent this efficient boundary layer pathway of energy cascade into the microscale. Enhanced dissipation at these stations is consistent with past findings of internal lee waves being generated over topography, radiating energy upward, and breaking (Nikurashin and Ferrari 2010; St. Laurent et al. 2012); the GM spectrum does not represent such a lee wave contribution, which has been shown to raise TKE dissipation rates to 10^{-8} W kg^{-1}. FSP estimates are too high in the main thermocline and above, and there is spatial variation in this

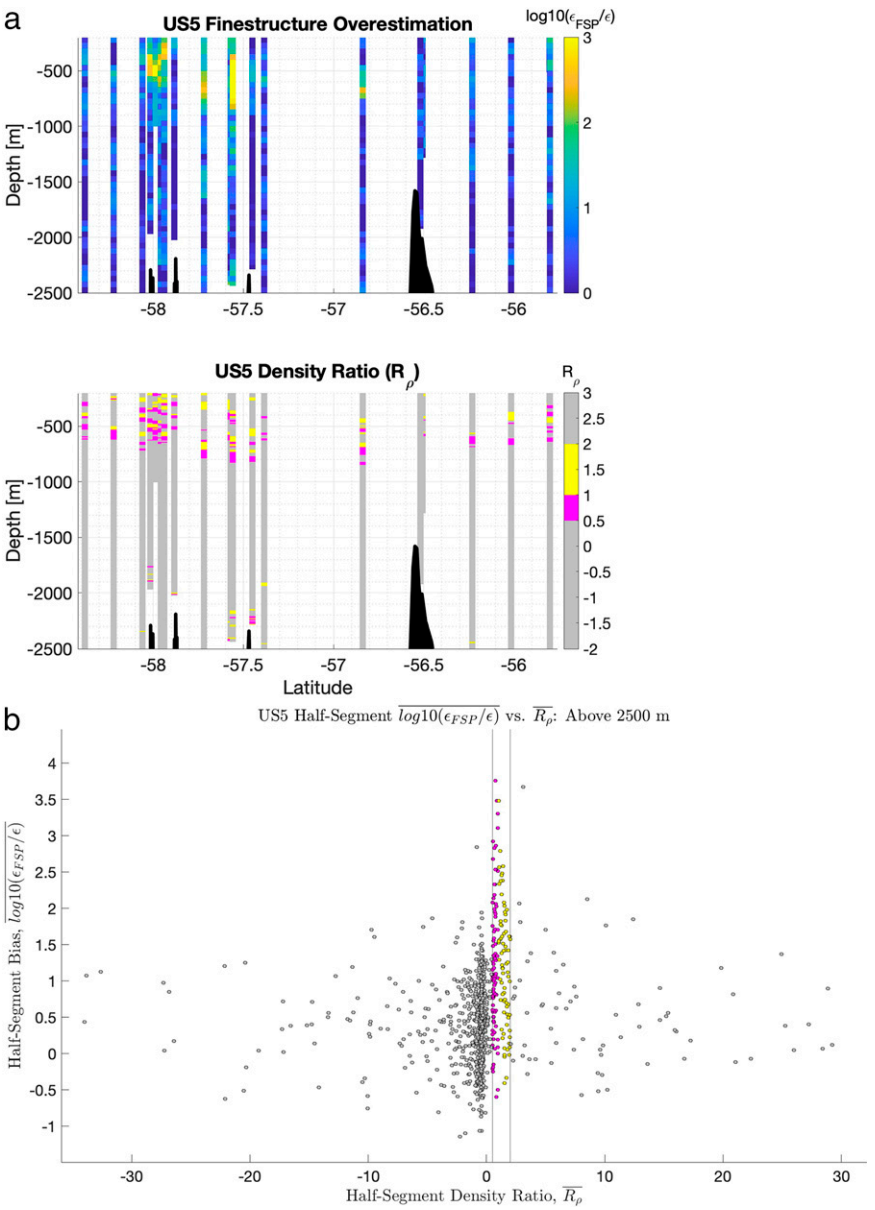

FIG. 7. (a) Overestimation of TKE dissipation rate by finescale strain parameterization (FSP) for upper 2500 m of DIMES US5 in comparison to density ratio, indicative of double diffusive instabilities (pink for diffusive regime and yellow for salt fingering regime). (b) Bias in FSP-estimated TKE dissipation rate $\log_{10}(\varepsilon_{\mathrm{FSP}}/\varepsilon)$ vs density ratio $R_\rho = (\alpha dT/dz)/(\beta dS/dz)$ for each half segment. Half segments where double diffusive instability is unlikely are colored gray. The water column is susceptible to the diffusive regime (pink) when $0.5 < R_\rho < 1$ and the salt fingering regime (yellow) when $1 < R_\rho < 2$. Both instabilities are possible near $R_\rho = 1$.

overestimation. For AUSSOM, the mild overestimation by FSP at shallower depths (Fig. 6a) is consistent with the same depth levels of DIMES US5 but varies intensely during the record, with severe bias before 3 December 2017. DIMES US5 and AUSSOM are fundamentally different because DIMES US5 sampled throughout the Drake Passage, while AUSSOM crossed into the PF on 28 November 2017 and remained in the PF's core through 23 December 2017. FSP methodology does not capture frontally intensified mixing processes active between 1 and 12 December 2017 (Fig. 6b), which are attributed to internal wave interactions. These are briefly addressed in Ferris et al. (2021, manuscript submitted to *J. Phys. Oceanogr.*) and have been investigated in a follow-on study (Ferris 2022) dedicated to the role of internal waves and frontal instability in downscale energy cascade in ACC jets.

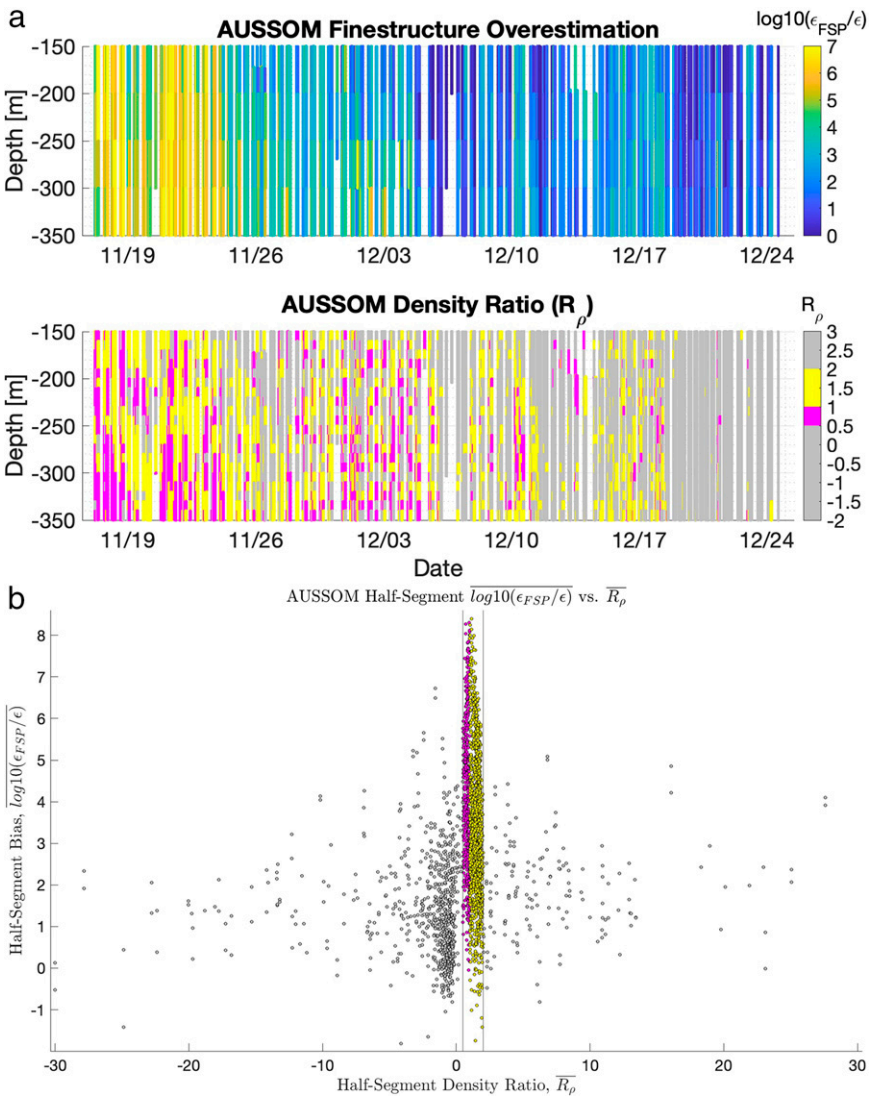

FIG. 8. (a) Overestimation of TKE dissipation rate by finescale strain parameterization (FSP) for AUSSOM in comparison to density ratio, indicative of double diffusive instabilities (pink for diffusive regime and yellow for salt fingering regime) (same as Fig. 7a). (b) Bias in FSP-estimated TKE dissipation rate $\log_{10}(\varepsilon_{\mathrm{FSP}}/\varepsilon)$ vs density ratio $R_\rho = (\alpha dT/dz)/(\beta dS/dz)$ for each half segment (same as Fig. 7b).

In the upper 2500 m of DIMES US5 (Fig. 7), FSP exhibits the greatest bias and there are more instances of doubly unstable stratification. This region around the PF (south of 57°) is known to be highly susceptible to *T*/*S* intrusions (Merrifield et al. 2016). The bias $\log_{10}(\varepsilon_{\mathrm{FSP}}/\varepsilon)$ and density ratio R_ρ for each segment in Fig. 7a are scattered in Fig. 7b. The worst biases (above 1.5 orders of magnitude) are collocated with unstable segments. This is repeated for AUSSOM (Fig. 8) and produces similar results. Segments corresponding to doubly unstable stratification are associated with biases of up to eight orders of magnitude (or 100 000 000 times the amount of TKE dissipating that is actually dissipating). Note this the compound error from all physical sources and cannot entirely be attributed to double diffusive instability.

The established practice for applying FSP to autonomous platforms is to average many available profiles for a given region to produce a climatological estimate for TKE dissipation rate. Ensemble averages with 90% bootstrapped confidence intervals are given for DIMES US5 and AUSSOM (Fig. 9). After Whalen et al. (2015) and other applications of FSP, for calculating confidence intervals the $\varepsilon_{\mathrm{FSP}}$ value for each half segment is treated as one sample. Contaminated segments, including the 50 m segments above and below each segment containing $0.5 < R_\rho < 2$, are removed from the left average (red) to produce the right average (green). Due to half-overlapping segments used to obtain $\varepsilon_{\mathrm{FSP}}$, a *T*/*S*-intrusive feature in a given 50 m half segment could theoretically contaminate the 50 m half segments above and below a

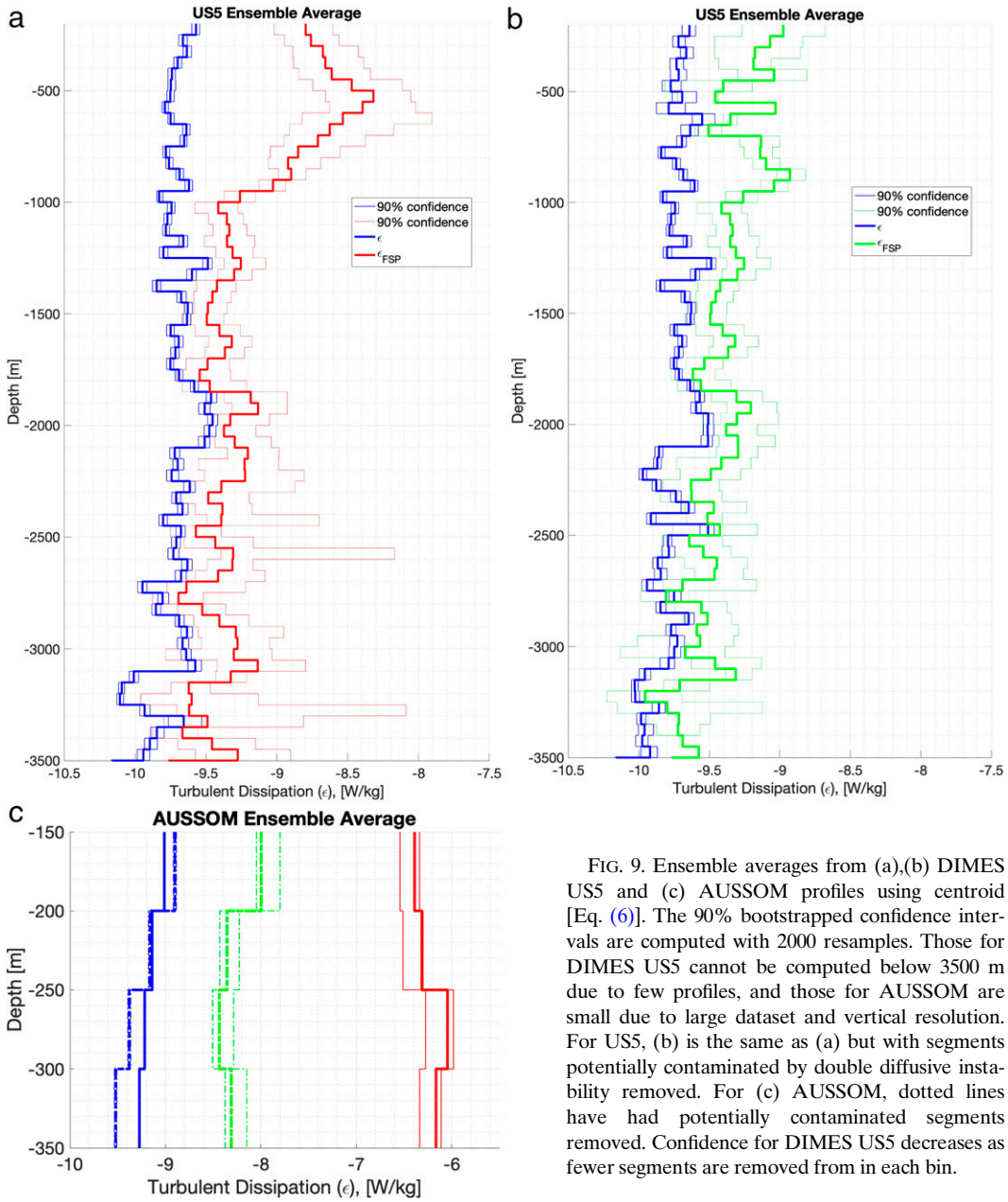

FIG. 9. Ensemble averages from (a),(b) DIMES US5 and (c) AUSSOM profiles using centroid [Eq. (6)]. The 90% bootstrapped confidence intervals are computed with 2000 resamples. Those for DIMES US5 cannot be computed below 3500 m due to few profiles, and those for AUSSOM are small due to large dataset and vertical resolution. For US5, (b) is the same as (a) but with segments potentially contaminated by double diffusive instability removed. For (c) AUSSOM, dotted lines have had potentially contaminated segments removed. Confidence for DIMES US5 decreases as fewer segments are removed from in each bin.

contaminated segment. (For Fig. 7 and Fig. 8, sensitivity analysis was performed to determine the effect of considering contamination in adjacent bins and its effects were found to be negligible.) Upon removing contaminated segments, DIMES US5 shows improvement by up to half an order of magnitude above 900 m but this is confounded by fewer measurements within each bin, widening confidence intervals. It is misleading to draw conclusions from the DIMES US5 profiles because eliminating contaminated segments from the average drastically reduces the number of profiles contributing to each bin, with sometimes only a single profile in a bin such that a confidence interval cannot be computed, for example the 550–650-m bin.

In contrast, the large sample size (739 profiles) of AUSSOM makes this a more reliable practice, and removing contaminated segments improves the ensemble average by approximately an order of magnitude. However, the ensemble average for $\varepsilon_{\mathrm{FSP}}$ remains one to two orders of magnitude higher than microstructure ε suggesting a remaining discrepancy due to assumption 2 and assumption 3. The remaining bias suggests implementation of depth-varying shear-to-strain ratio R_ω might be appropriate, contrary to the general practice of choosing a constant R_ω. Similarly, departure in the Southern Ocean internal wave spectrum from the GM spectrum could explain the residual overestimation by FSP. The GM spectrum does not account for enhanced

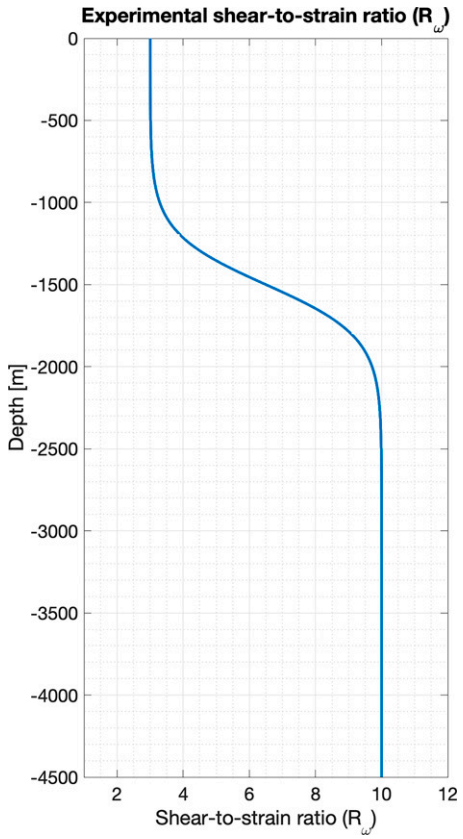

FIG. 10. Experimental depth-varying shear-to-strain ratio used to produce Fig. 11. This is a hybrid of G-M theory $R_\omega = 3$ and the inertial oscillation-enhanced $R_\omega = 10$ and has equation $R_\omega(z) = 3.5\tanh[2\pi(z - 1500)/2000] + 6.5$.

internal lee wave content in the Southern Ocean produced by strong geostrophic flow impinging on complex topography. In the future, it may be worth employing a methodology leveraging alternative spectral presentations as motivated by stratified turbulence literature.

4. Discussion

For both DIMES US5 and AUSSOM, we have used FSP to estimate TKE dissipation rate from CTD and compared to direct microstructure measurements to show that double diffusive instabilities are associated with large biases. Double diffusive instabilities contaminate FSP, compounding with other sources of bias to estimate up to 100 000 000 times more TKE dissipation in the PF the ocean than actually occurs. Strain-based methodology (FSP) is vulnerable to failure in intrusive water mass regions and likely falls outside the widely reported agreement factor of 2–3 in frontal regions of the global ocean where double diffusive instabilities are active. This is notable because the community might otherwise consider applying FSP as is to CTD from the international Argo program to solve ocean mixing problems. Sites of elevated TKE dissipation as estimated from Argo floats (Whalen et al. 2015) are often collocated with frontal regions where frontal physics might contaminate the internal wave-associated strain spectrum with a double diffusive instability spectrum. In other words, the observed strain spectrum attributed to internal waves is convolved with a second strain spectrum attributable to double diffusive instabilities. Recall that the core assumptions of FSP are that observed strain-like features are internal wave strain (assumption 1), the internal wave spectrum is well represented by the GM spectrum (assumption 2), and downscale energy transfer steadily occurs via nonlinear wave–wave interactions such that for a control volume the production of TKE by shear matches the dissipation by molecular viscosity and buoyancy flux (assumption 3). As such, FSP [Eq. (1)] violates assumption 1 and should be paired with an R_ρ-based data selection rule when applied anywhere in the ocean, especially frontal regions. Succinctly, FSP should not be performed when R_ρ indicates that double diffusive instabilities are possible.

Assumption 3 is difficult to assess with the high-resolution data available (e.g., AUSSOM does not have associated velocity measurements) which leaves us to speculate about assumption 2, that the constant shear-to-strain ratio chosen from the literature ($R_\omega = 10$) reasonably represented the aspect ratio of the internal wave spectrum in all parts of the water column. We recall that if the true shear-to-strain ratio is lower than the assumed constant R_ω in any part of the water column, $\varepsilon_{\mathrm{FSP}}$ will be an overestimate of true TKE dissipation rate ε. Furthermore, the physical mechanism justifying high shear-to-strain ratio (bottom-intensified inertial oscillations) in Nikurashin and Ferrari (2010) should become less dominant away from the bottom boundary. We test a shear-to-strain ratio $R_\omega(z)$ which smoothly transitions from the GM-assumed $R_\omega = 3$ above 1000 m to the literature-supported $R_\omega = 10$ below 2000 m (Fig. 10). FSP is repeated for both DIMES US5 and AUSSOM and the ensemble averages resulting from this exercise are shown in Fig. 11. For US5 (which is less contaminated by double diffusive instability, relative to AUSSOM) the ensemble average for $\varepsilon_{\mathrm{FSP}}$ collapses onto the true ensemble average. The ensemble average for AUSSOM improves by two orders of magnitude. Repeating Fig. 9, averages with doubly unstable segments removed are provided on the right in green. Drawing conclusions from DIMES US5 is once again precarious (due to few available profiles remaining in each 50-m bin in and above the main thermocline) but both DIMES US5 and AUSSOM show meaningful improvement. Section plots with the transitional $R_\omega(z)$ and doubly unstable segments removed are provided in Fig. 5 and Fig. 6. Removal of doubly unstable segments substantially restricts the amount of data available for FSP, but to the benefit of markedly improved $\varepsilon_{\mathrm{FSP}}$.

The Southern Ocean deviates from the GM spectrum in the deep because it has a steady zonally uninhibited current impinging on underling seamounts to produce its own internal wave spectrum with internal lee wave origins. It is straightforward to substantiate the apparent deep ocean $R_\omega = 10$ by substituting anticipated internal lee wave frequencies into the

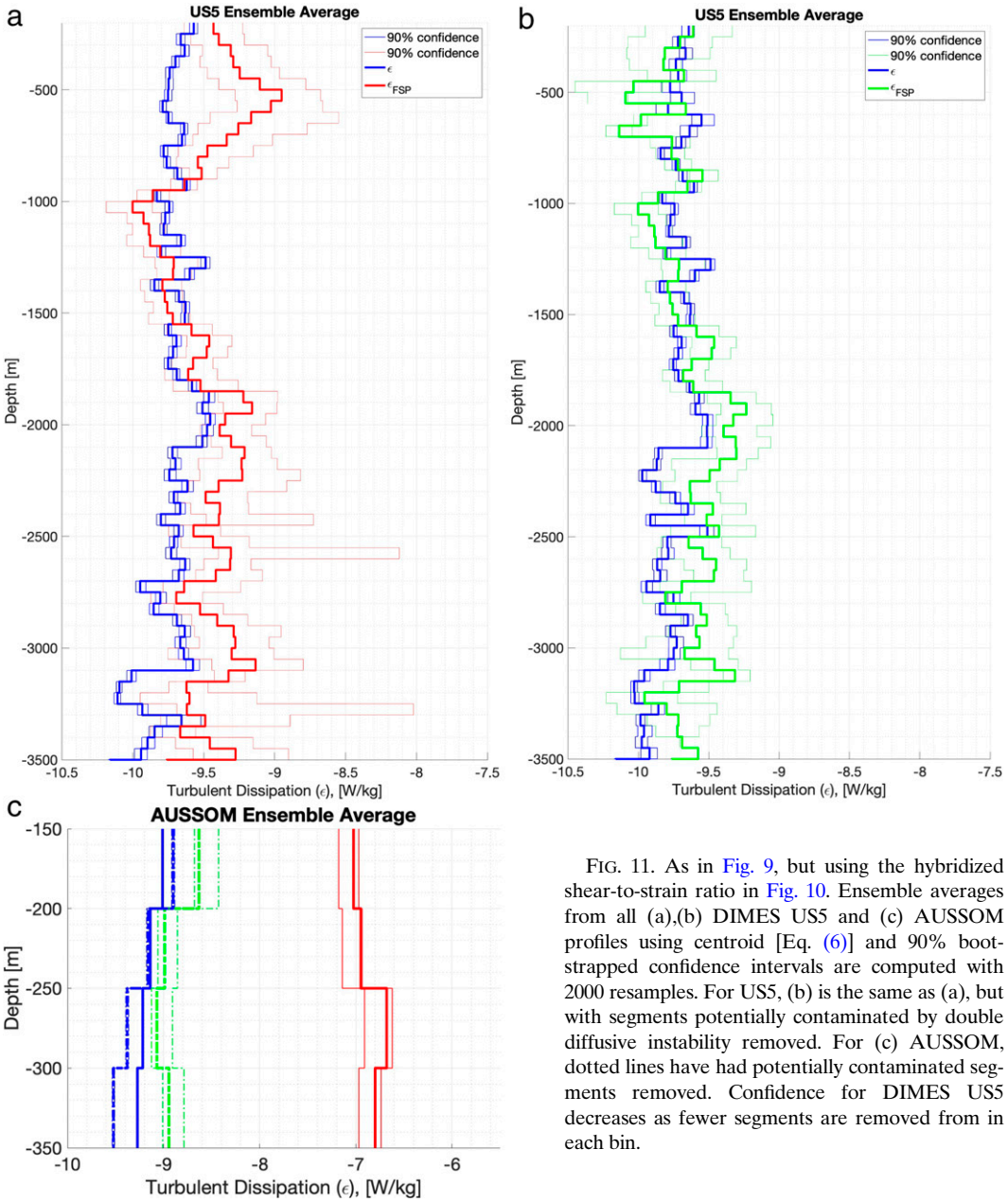

FIG. 11. As in Fig. 9, but using the hybridized shear-to-strain ratio in Fig. 10. Ensemble averages from all (a),(b) DIMES US5 and (c) AUSSOM profiles using centroid [Eq. (6)] and 90% bootstrapped confidence intervals are computed with 2000 resamples. For US5, (b) is the same as (a), but with segments potentially contaminated by double diffusive instability removed. For (c) AUSSOM, dotted lines have had potentially contaminated segments removed. Confidence for DIMES US5 decreases as fewer segments are removed from in each bin.

ratio of the IW shear to strain variance for a single wave (Polzin et al. 1995),

$$\frac{\left\langle V_z^2 \right\rangle}{N^2 \left\langle \xi_z^2 \right\rangle} = \frac{(\omega^2 + f^2)(N^2 - \omega^2)}{N^2(\omega^2 - f^2)} = R_\omega, \tag{7}$$

where $\left\langle V_z^2 \right\rangle$ is the shear variance. Using the mean Coriolis frequency for DIMES US5, an assumed ocean velocity of $U = 0.1$ m s^{-1}, and observed stratification (Fig. 12a), internal waves can exist fin the depth range of $785 < 2\pi/k < 5235$ m for the deep ocean and down to 315 m in the main thermocline. The range of shear-to-strain ratios [Eq. (7)], which can exists for possible IW frequencies are given in Fig. 12b. Near-internal oscillations have a higher shear-to-strain ratio (R_ω) and can exist in the deep ocean, consistent with Nikurashin and Ferrari's (2010) explanation of high R_ω in the deep Southern Ocean. It makes sense that inertial oscillations have larger shear because their motion is predominately in the horizontal direction; there is higher level of kinetic energy with minimal actual raising of fluid.

To better contextualize these results to Argo-based FSP (which is a subject of broad community interest), we applied FSP to Argo profiles (Fig. 13a) in region of AUSSOM and DIMES from 2010 through 2020. This was done using 100-m segments from 200 to 2000 m and $R_\omega = 10$ as before, for which

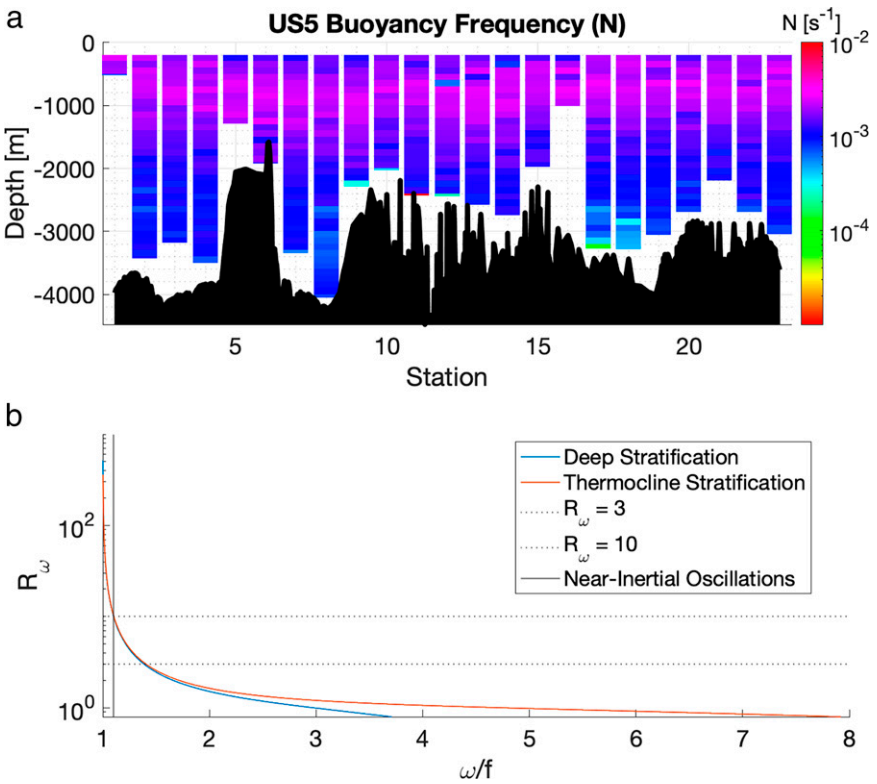

FIG. 12. (a) Stratification for DIMES US5 and (b) estimated shear-to-strain ratios for range of possible internal waves for deep ocean and main thermocline.

an example strain spectrum is given (Fig. 14a). While the Argo program has shifted to deploying floats with 1–2-m vertical resolution, some older floats with coarser resolution are found in the dataset. We consider "good data only" (specified by the Coriolis GDAC interface) over the upper 1000 m, below which many floats assume coarser vertical sampling, and eliminate additional floats which transition to coarse sampling above this depth. [To preserve battery while providing adequate hydrographic coverage, the Argo program agreed on a vertically nonuniform sampling scheme; this variable and sometimes coarse sampling resolution of Argo floats is what outright prevents their compatibility with Thorpe scale analysis (MacKinnon et al. 2009).] Were this not done, it would be precarious to use the fixed high wavenumber cutoff of 10 m; coarse sampling muddles the demarcation between signal and noise near the spectral rolloff. To be clear, this is not the same collection of Argo profiles used by Whalen et al. (2012, 2015) nor an identical application of FSP. Therefore, TKE dissipation values should not be directly compared between studies.

TKE dissipation rates for each profile are shown in Fig. 13b, along with associated susceptibility to *T*/*S*-intrusive features (Fig. 13c). The full Argo dataset has fewer segments with density ratios indicative of double diffusive instabilities relative to DIMES US5 and AUSSOM, which is to be expected because the latter two studies were both designed to sample in and around the ACC fronts (and thus likely to capture *T*/*S*-intrusive features) contrary to the quasi-random sampling of Argo. The high TKE-dissipation patches around profiles 50 and 550 (Fig. 13b) are believed to be real and associated with frontal features or eddies from their TKE dissipation structure. In the absence of collocated microstructure measurements, we make a similar plot to Figs. 7b and 8b with $\varepsilon_{\mathrm{FSP}}$ presented as a relative magnitude $\overline{\log10[\varepsilon_{\mathrm{FSP}}/(5\times10^{-9})]}$ rather than a true bias $\overline{\log10(\varepsilon_{\mathrm{FSP}}/\varepsilon)}$; a normalization value corresponding to when the buoyancy Reynolds number $\mathrm{Re} = \varepsilon/\nu N^2$ takes on a value of 200, a baseline for turbulence of sufficient strength to be isotropic (Gargett et al. 1984). This is for the purpose of exploring the potential impact of *T*/*S*-intrusive features on the magnitude of Argo-based FSP in the Southern Ocean. Figure 15a shows these magnitudes versus density ratio for a DIMES US5-region subset, an AUSSOM-region subset, and the full region, created using ocean_data_tools (Ferris 2020). Few *T*/*S*-intrusive features were captured by the DIMES US5 or AUSSOM subsets, but more were captured in the full-region dataset. Though not all *T*/*S*-intrusive segments are associated with high values of $\varepsilon_{\mathrm{FSP}}$, the largest estimates are associated with *T*/*S*-intrusive features. The test for *T*/*S*-intrusive density ratio (yellow or magenta points) in Fig. 15a shows the average *T*/*S*-intrusive density ratio ($0.5 < R_\rho < 2$) if present at all in the segment. Not all yellow and magenta points correspond to high $\varepsilon_{\mathrm{FSP}}$, unlike Figs. 7b and 8b. This is for three reasons: 1) the density ratio test for double diffusive instability is binary and thus

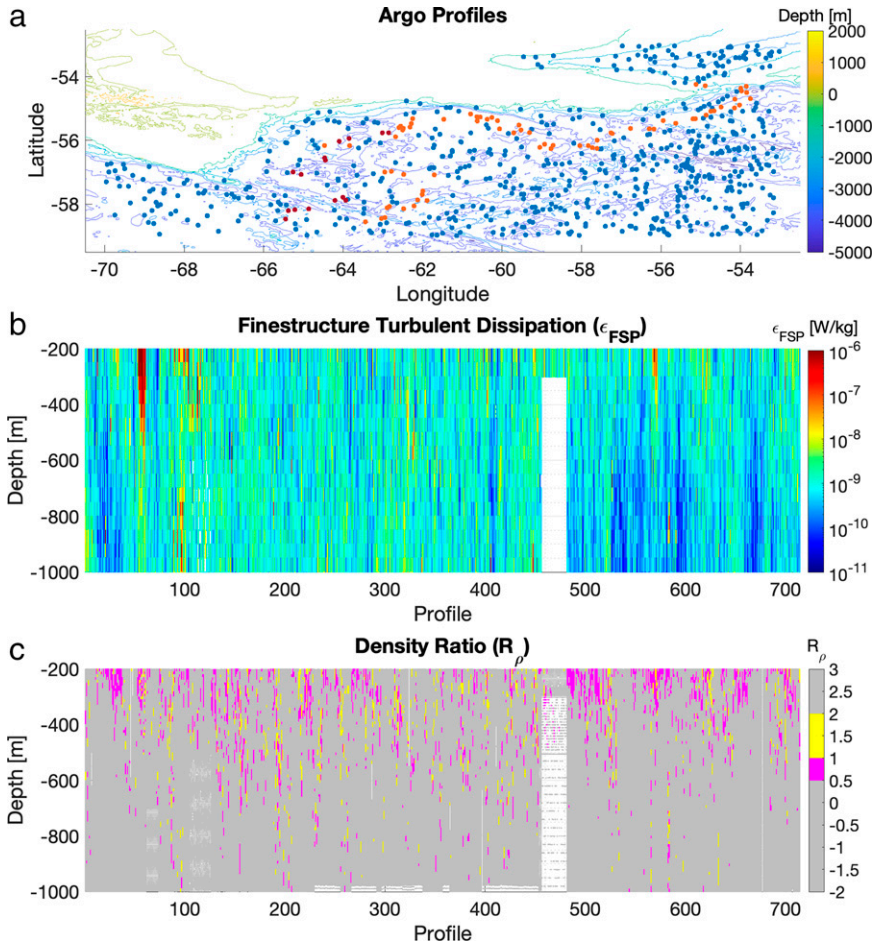

FIG. 13. (a) Argo profiles from 2010 through 2020 in region of study (all colors), with subsets for the regions of DIMES US5 (scarlet) and AUSSOM (orange). (b) FSP-estimated TKE dissipation rate with $R_\omega = 10$. (c) Density ratio $R_\rho = (\alpha dT/dz)/(\beta dS/dz)$ for each segment (pink for diffusive regime and yellow for salt fingering regime).

agnostic of the number of doubly unstable features in a particular profile segment, 2) the density ratio measures favorability to double diffusive instability and not the presence of *T*/*S* intrusions, and 3) the *y* axis in Fig. 15a is a measure of magnitude and not bias—small-magnitude segments could have very large bias if the true ε for the segment was also small.

For the Argo array, subtle data quality issues present a second source of bias which appears almost identical to *T*/*S*-intrusive features but is an artifact in the observations. An example is presented in Fig. 16, which shows vertical profiles from an Argo float which is experienced sensor issues but passed automated Argo quality checks and was distributed as "good data." An issue with the conductivity sensor produced erroneous density features with the same vertical scale as both *T*/*S* intrusions and true internal wave strain (Fig. 15a). The consequences of this and similar CTD issues (a reality of long-deployed and unsupervised platforms) are large; Fig. 15b shows an arithmetic mean for the full Argo dataset with (blue dotted) and without (gray dotted) the float in question. This illustrates the danger of applying FSP to the global Argo array in an automated fashion, even if the practitioner limits the dataset to "good data only."

At this point we wish to underscore the distinction between overestimating TKE dissipation rate (ε) and overestimating diffusivity, $K_\rho = \Gamma\varepsilon/\overline{N}^2$. Regions prone to double diffusive convective regimes which are biased high in TKE dissipation rate are not biased equivalently high in diffusivity (K_ρ) because double diffusive convective mixing regimes are energetically more efficient that 3D isotropic turbulence at converting kinetic energy to potential energy.

Ensemble centroids for the Argo subsets and full-region dataset are given in (Fig. 15b), and we turn our attention to the nuances of averaging [Eq. (6)]. The ensemble centroids in Figs. 9, 11, and 15 are geometric means. Geometric means (calculated by applying logarithmic transformation prior to averaging) are appropriate for representing the centroid of a dataset where data points vary logarithmically, but arithmetic means (no logarithmic transformation prior to averaging) are

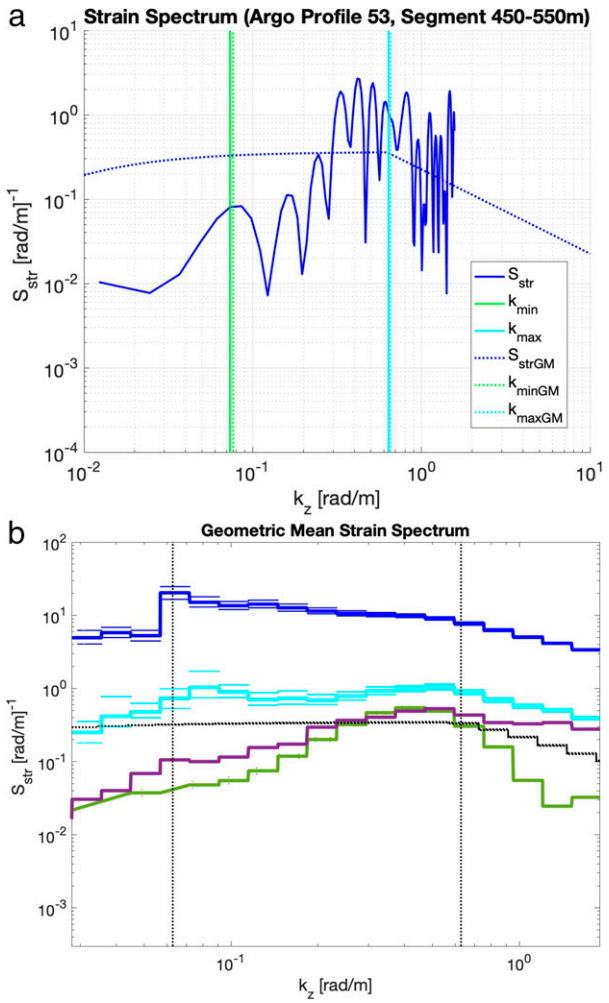

FIG. 14. (a) Example strain spectra and limits of integration [Eq. (4)] for one segment of Argo, as in Fig. 3. The segment has 2-m vertical resolution in CTD data. (b) Geometric mean strain spectra for all depth levels of AUSSOM glider (blue), DIMES US5 VMP (green), and Argo (purple) datasets with 90% confidence intervals. The mean strain spectrum for the doubly stable region of AUSSOM (after 0000 UTC 19 Dec 2017) is also provided (cyan).

not. The order of logarithmic transformation and averaging determines whether an estimated TKE dissipation rate is simply the maximum value of a given ensemble (arithmetic mean) or whether it is the centroid of all TKE dissipation estimates in the ensemble (geometric mean). Given that *T*/*S* intrusive features appear as artificial internal-wave-attributed strain and bias ε_{FSP} to be high, the consequences of including these features in an arithmetic mean (dotted blue line in Fig. 15b) are more deleterious than including them in a geometric mean (solid blue line in Fig. 15b). While *T*/*S*-intrusive features are not dominate in the global ocean, they exist and can create large biases in ε_{FSP}. To ameliorate this, one should use a geometric mean and/or remove the contaminated segments when attempting FSP analysis; *T*/*S*-intrusive features have the potential to introduce large errors if included in either a geometric mean with little contamination but few samples (as in DIMES US5), a geometric mean with much contamination and many samples (as in AUSSOM), or an arithmetic mean of any kind (as in the Argo full-region dataset).

Upon examining ε_{FSP} derived from Argo profiles, it is reasonable to wonder why AUSSOM (with its superior vertical resolution) had high bias (Fig. 8a) relative to the other datasets, some of which remained even after adjusting the shear-to-strain ratio and removing contaminated segments (Fig. 11c). A well-documented issue in the glider-based CTD is thermal lag, which arises from the displacement between the thermistor and conductivity cell within a CTD, as well as the thermal inertial of the cell itself. As a glider dives or climbs through sharp gradients, there is a mismatch between temperature and salinity, which can produce erroneous density features [there are excellent examples, such as Garau et al. (2011) or Latarius et al. (2019)]. Thermal lag acts at 1–10-m scale, which falls within the same narrowband finescale structure as *T*/*S*-intrusive features and oceanic internal waves. As such, it was important to verify that the thermal lag was not the source of the high strain variance within the *T*/*S*-intrusive region of AUSSOM. We applied thermal lag correction after Garau et al. (2011) using https://github.com/socib/glider_toolbox, which is showing in Fig. 17 (dotted lines). We also visually inspected temperature, conductivity, salinity, and density profiles. Given that mirroring in adjacent casts is found in both temperature and salinity, is not removed by thermal lag correction, and is consistent with observations of internal waves, we attribute these features to be produced by internal waves aliased with the frequency of glider up- and downcasts. Regarding AUSSOM and why the associated FSP dissipation estimates are still too high after decontaminating: the large biases in AUSSOM are likely intrusive features combined with an intense internal wavefield, which perhaps does not dissipate locally (via radiation away or momentum transfer into the mean flow, violating assumption 3).

Finally, worth discussing are the nuances of the glider, VMP, and Argo float platforms and their impacts on the observed strain spectra. The mean AUSSOM spectra (Fig. 14b) is closer to a GM shape than DIMES US5 or Argo, we think it is because it is the upper ocean and relatively immune to the non-GM physics of the ACC at depth. Its magnitude varies inside and outside of the front; the mean AUSSOM spectra for the doubly stable region (19 December and beyond) is over an order of magnitude lower than that for the full AUSSOM dataset which is dominantly in the front and contaminated by *T*/*S*-intrusion-like features.

Individual Argo spectra generally have a spectral shape similar to the example spectrum in Fig. 14a, with less strain power in low wavenumbers relative to AUSSOM or DIMES US5. We are unable to determine the cause of this distinctive spectral shape for Argo with our dataset. However, we speculate that it is either due to a physical reason (e.g., the Argo floats primarily sample the open ocean away from the front, which is less likely to have a GM spectra than the Drake Passage) or a technical reason (e.g., an engineering property specific to the platform causes this). We suspect a

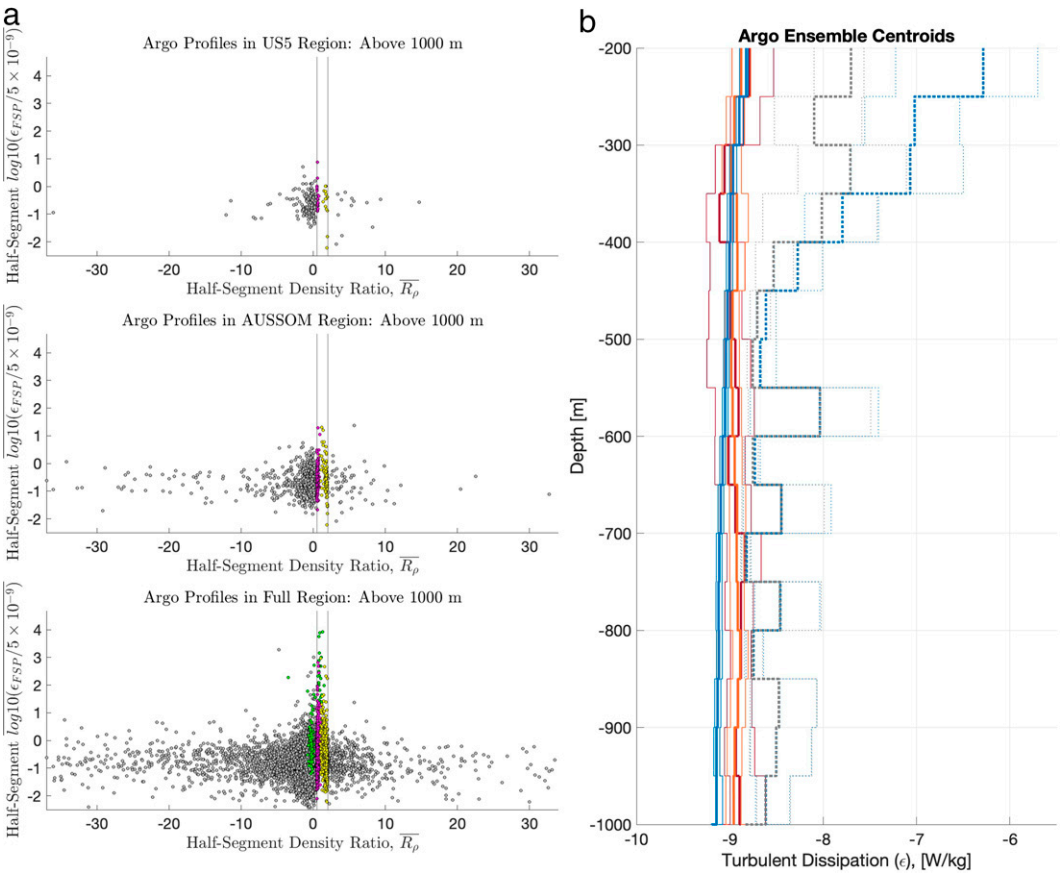

FIG. 15. (a) As in Figs. 7b and 8b, but with y axis as FSP-estimated TKE dissipation rate relative to $\varepsilon = 5 \times 10^{-9}$ W kg^{-1}. Segments from a float with suspected CTD issues (ID: 1901892), distributed as good data, are highlighted green. (b) Ensemble geometric means with 90% confidence intervals (solid lines) corresponding to Fig. 13a, with a full-region arithmetic mean (blue dotted lines). The arithmetic mean is recalculated (gray lines) without the green float, which accounted for 9 of 714 profiles. Yellow and magenta correspond to segment density ratio (Fig. 13c).

technical reason that Argo floats could be problematic is that Argo floats are ballasted to be near-neutral buoyancy, fall slowly, and have little inertia. We speculate that the strain spectrum is depleted in low wavenumbers because the Argo floats are missing low wavenumbers; moving with the longest internal waves instead of measuring their associated strain. The fluid–structure interaction of Argo floats could act as a natural filter to remove certain wavenumbers. However, this is only a conjecture. The different datasets cover different regions and times in the Southern Ocean using different sensors. We simply do not know enough to ascertain the truth about the different spectral shapes at this time. This issue deserves additional future investigation.

A final note is that glider users should pay attention to aliasing and statistical independence when applying FSP to glider datasets. In this paper, our aim was to examine the efficacy of FSP from a technical perspective. When implementing glider-based FSP to obtain an actual TKE dissipation rate or diffusivity, averaging 10 consecutive profiles implies that the glider is resampling the same feature or water column several times in a row and these are not truly 10 independent estimates. Thus, applying FSP to 10 consecutive profiles does not produce 10 statistically independent estimates of ε in a region and should be avoided when possible.

5. Conclusions

The application of FSP to estimate TKE dissipation in the Southern Ocean has several layers of vulnerability rooted in the method's assumptions. To summarize, the most tractable vulnerability to address is observed T/S features (both double diffusive instabilities and CTD issues) being misidentified as internal wave strain. Even if these features are removed, the second layer is that shear-to-strain ratio (R_ω) is well documented to vary by more than an order of magnitude throughout the global ocean (producing an error of up to an order of magnitude) and can no longer justifiably be assumed to have a constant value. Finally, even if the R_ω is correctly calibrated, the innermost vulnerability (and most difficult to correct) is that the parameterization assumes the validity of a GM spectrum. With its near spatial universality, basing finescale parameterizations on the GM spectrum to solve global mixing

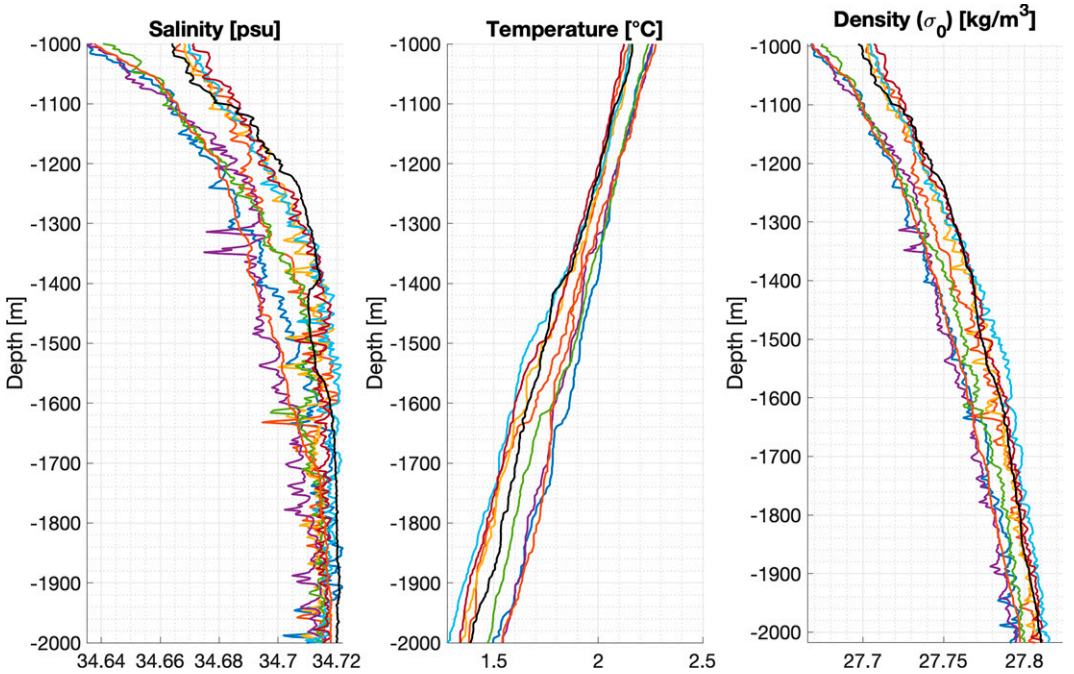

FIG. 16. Profiles from the Argo float (ID: 1901892) with suspected CTD issues, which corresponds to erroneous doubly diffusive segments (green dots) in Fig. 15. The conductivity sensor appears to become erratic at a depth of 1200 m while ascending (black line), perhaps due to intake of biological material, and remain so (colored profiles).

problems seems like an innocuous assumption. However, the spatial scale of specific energetic regions (such as the ACC) are not directly proportional to their importance; TKE dissipation varies by orders of magnitude such that its extreme values contribute disproportionately more to ocean mixing than its mean values. The GM spectrum may fail in limited regions of the ocean, but these limited regions of the ocean could be responsible for the majority of the turbulent mixing. Practitioners of FSP may potentially be taking the wrong approach by applying uniform internal wave physics to understand, calculate, and build simulations of a spatially heterogenous process. FSP is useful tool for estimating TKE dissipation rates in many parts of the ocean where internal waves dominate, but it should not be taken as a mathematical truth or the bridge to increment our understanding of the turbulence-associated physics.

Frontal physics (as well as data quality issues) mimic the role of internal wave strain. When applying FSP to data from the global Argo array, we must be cautious of data collected in any strong frontal region. The frontal physics discussed in this paper are not unique to the ACC and extend to global areas such as the Kuroshio, Agulhas Current, and Gulf Stream. Referencing the Argo-derived global map of estimated TKE dissipation rate (Fig. 3 of Whalen et al. 2015), it is noticeable that estimated rates are sharply enhanced ($\varepsilon \gg 1 \times 10^{-8}$ W kg^{-1}) in these frontal regions as well as much of the northwest Pacific gyre. We wonder whether the TKE estimates in each of these regions are inflated by frontal physics, data quality issues, or truly due to enhanced internal wave activity. A second quandary is whether an enhanced internal wavefield results in an enhanced TKE dissipation. This hinges on the assumption that the internal wavefield is locally dissipative such that at any given location there is leakage of the internal wave spectrum as TKE dissipation (ε). In the case of the Southern Ocean, St. Laurent et al. (2012) found that the most unstable lee wave energy dissipated within the bottom 1000 m of topography, while the lower-mode energy in the spectrum escapes upward to produce the Southern Ocean internal wavefield and circulates around the upper ocean (thermocline and above). Whether this energy dissipates locally or propagates adiabatically without dissipation until encountering a catalyst such as wave–mean flow interaction (restated, the amount of decoupling between the finescale and the microscale) is a key future research question.

The conclusions of this study are that 1) FSP should not be conducted where double diffusive instabilities are active, 2) an appropriate shear-to-strain ratio R_ω should be tuned from available microstructure data for each distinct region of the global ocean prior to performing FSP, 3) choose the appropriate averaging scheme for FSP-estimated TKE dissipation rate (i.e., arithmetic versus geometric mean), 4) subtle data quality issues are an insidious source of bias when applying FSP to automatically quality-controlled data products, and 5) free-falling platforms with a high vertical sampling resolution (such as autonomous underwater gliders) allow the user to integrate over more of the strain spectrum while avoiding the dissipation scale at $k_{\max} > k_c$ (unlike ship-lowered CTD which has a spectral rolloff muddled by heave or Argo which often cannot measure strain down to the 1-m scale). These results are broadly applicable to energetic currents rich in

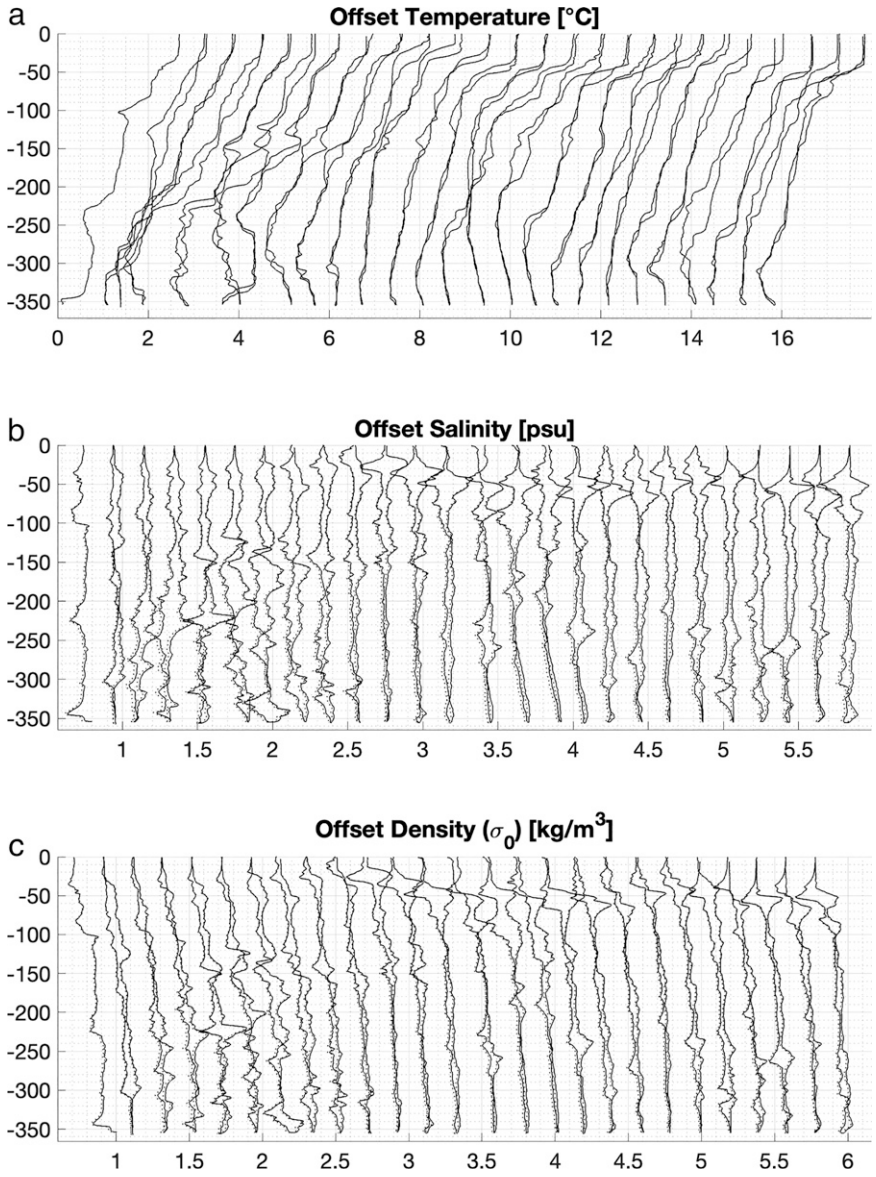

FIG. 17. Glider profiles during AUSSOM, corresponding to 2032 UTC 1 Dec through 0712 UTC 3 Dec 2017 in which the glider was in the core of the Polar Front and observed elevated TKE dissipation rates. Showing (a) offset temperature, (b) offset salinity, and (c) offset density. Adjacent upcasts and downcasts are paired, and the same variables corrected for thermal lag are provided (dotted lines) for reference.

frontal structure and anywhere *T*/*S*-intrusive regimes are active. To accurately understand global patterns of mixing—especially in frontal zones, we are best served using direct turbulence measurements. Large-eddy simulation (LES) numerical studies are another tool to explore estimates of mixing rates from the finescale energy cascade (Khani 2018), and advances in theoretical understanding or computational capacity could enable better future fine structure estimates of turbulent mixing.

Autonomous platforms (VMP, gliders, floats) allow for potentially effective applications of FSP with the caveat that, because of their enhanced resolution, we now have the responsibility to check for double diffusive instabilities. As such, the community has several choices to deal with this going forward: to apply more rigorous quality control to Argo-derived TKE dissipation rate estimates, add shear probes to floats, or dramatically increase the number of microstructure-equipped glider surveys of frontal regions. The problem with this first option is that FSP can only capture the processes we have designed it to capture. The second presents a technical challenge of implementing durable and biofouling-proof shear probes (which is not yet possible). The third option (true microstructure measurements) is likely the

most economical and rewarding, has the highest level of technical readiness, and would elucidate undiscovered nuances of forward energy cascade, which the community is still tackling.

Acknowledgments. This paper is VIMS Contribution No. 4065. Computational resources were provided by the VIMS Ocean–Atmosphere and Climate Change Research Fund. AUSSOM was supported by the OCE Division of the National Science Foundation (NSF); we thank the crew of the R/V *Gould* for their support during the field program, and Justin Shapiro for glider recovery. DIMES US5 was supported by NSF; we thank the crews on the R/V *Palmer*. Argo data were collected and made freely available by the Coriolis project and contributive programs (http://www.coriolis.eu.org).

Data availability statement. All AUSSOM and DIMES US5 data used in the paper will be shared at microstructure.ucsd.edu, the NSF-funded Microstructure Database.

REFERENCES

Alford, M. H., and R. Pinkel, 2000: Observations of overturning in the thermocline: The context of ocean mixing. *J. Phys. Oceanogr.*, **30**, 805–832, https://doi.org/10.1175/1520-0485(2000)030<0805:OOOITT>2.0.CO;2.

Bartello, P., and S. M. Tobias, 2013: Sensitivity of stratified turbulence to the buoyancy Reynolds number. *J. Fluid Mech.*, **725**, 1–22, https://doi.org/10.1017/jfm.2013.170.

Beaird, N., I. Fer, P. Rhines, and C. Eriksen, 2012: Dissipation of turbulent kinetic energy inferred from Seagliders: An application to the eastern Nordic seas overflows. *J. Phys. Oceanogr.*, **42**, 2268–2282, https://doi.org/10.1175/JPO-D-12-094.1.

Bell, T. H., Jr., 1975: Topographically generated internal waves in the open ocean. *J. Geophys. Res.*, **80**, 320–327, https://doi.org/10.1029/JC080i003p00320.

Brearley, J. A., K. L. Sheen, A. C. Naveira Garabato, D. A. Smeed, and S. Waterman, 2013: Eddy-induced modulation of turbulent dissipation over rough topography in the Southern Ocean. *J. Phys. Oceanogr.*, **43**, 2288–2308, https://doi.org/10.1175/JPO-D-12-0222.1.

Cael, B. B., and A. Mashayek, 2021: Log-skew-normality of ocean turbulence. *Phys. Rev. Lett.*, **126**, 224502, https://doi.org/10.1103/PhysRevLett.126.224502.

Chinn, B. S., J. B. Girton, and M. H. Alford, 2016: The impact of observed variations in the shear-to-strain ratio of internal waves on inferred turbulent diffusivities. *J. Phys. Oceanogr.*, **46**, 3299–3320, https://doi.org/10.1175/JPO-D-15-0161.1.

Dillon, T. M., 1982: Vertical overturns: A comparison of Thorpe and Ozmidov length scales. *J. Geophys. Res.*, **87**, 9601–9613, https://doi.org/10.1029/JC087iC12p09601.

Ferrari, R., and C. Wunsch, 2009: Ocean circulation kinetic energy: Reservoirs, sources, and sinks. *Annu. Rev. Fluid Mech.*, **41**, 253–282, https://doi.org/10.1146/annurev.fluid.40.111406.102139.

Ferris, L., 2020: ocean_data_tools: A MATLAB toolbox for interacting with bulk freely-available oceanographic data. *J. Open Source Software*, **5**, 2497, https://doi.org/10.21105/joss.02497.

——, 2022: Across-scale energy transfer in the Southern Ocean. Ph.D. dissertation, Dept. of Physical Sciences, Virginia Institute of Marine Science, William and Mary, 190 pp.

——, D. Gong, T. Ijichi, S. T. Merrifield, J. Shapiro, and L. St. Laurent, 2020: Turbulent dissipation rate and mixing variations in the polar front of the Southern Ocean. *Ocean Sciences Meeting 2020*, San Diego, CA, Amer. Geophys. Union, PS51A-04, https://agu.confex.com/agu/osm20/meetingapp.cgi/Paper/648069.

Frants, M., G. M. Damerell, S. T. Gille, K. J. Heywood, J. MacKinnon, and J. Sprintall, 2013: An assessment of density-based finescale methods for estimating diapycnal diffusivity in the Southern Ocean. *J. Atmos. Oceanic Technol.*, **30**, 2647–2661, https://doi.org/10.1175/JTECH-D-12-00241.1.

Garau, B., S. Ruiz, W. G. Zhang, A. Pascual, E. Heslop, J. Kerfoot, and J. Tintoré, 2011: Thermal lag correction on Slocum CTD glider data. *J. Atmos. Oceanic Technol.*, **28**, 1065–1071, https://doi.org/10.1175/JTECH-D-10-05030.1.

Gargett, A. E., 1990: Do we really know how to scale the turbulent kinetic energy dissipation rate ε due to breaking of oceanic internal waves? *J. Geophys. Res.*, **95**, 15 971–15 974, https://doi.org/10.1029/JC095iC09p15971.

——, and T. Garner, 2008: Determining Thorpe scales from ship-lowered CTD density profiles. *J. Atmos. Oceanic Technol.*, **25**, 1657–1670, https://doi.org/10.1175/2008JTECHO541.1.

——, T. R. Osborn, and P. W. Nasmyth, 1984: Local isotropy and the decay of turbulence in a stratified fluid. *J. Fluid Mech.*, **144**, 231–280, https://doi.org/10.1017/S0022112084001592.

Gill, A. E., 1982: *Atmosphere-Ocean Dynamics*. Academic Press, 662 pp.

Gregg, M. C., 1989: Scaling turbulent dissipation in the thermocline. *J. Geophys. Res.*, **94**, 9686–9698, https://doi.org/10.1029/JC094iC07p09686.

——, and E. Kunze, 1991: Shear and strain in Santa Monica basin. *J. Geophys. Res.*, **96**, 16 709–16 719, https://doi.org/10.1029/91JC01385.

Huussen, T. N., A. C. Naveira Garabato, H. L. Bryden, and E. L. McDonagh, 2012: Is the deep Indian Ocean MOC sustained by breaking internal waves? *J. Geophys. Res.*, **117**, C08024, https://doi.org/10.1029/2012JC008236.

Johnston, T. S., and D. L. Rudnick, 2015: Trapped diurnal internal tides, propagating semidiurnal internal tides, and mixing estimates in the California Current System from sustained glider observations, 2006–2012. *Deep-Sea Res. II*, **112**, 61–78, https://doi.org/10.1016/j.dsr2.2014.03.009.

Khani, S., 2018: Mixing efficiency in large-eddy simulations of stratified turbulence. *J. Fluid Mech.*, **849**, 373–394, https://doi.org/10.1017/jfm.2018.417.

——, and M. L. Waite, 2013: Effective eddy viscosity in stratified turbulence. *J. Turbul.*, **14**, 49–70, https://doi.org/10.1080/14685248.2013.837913.

Kimura, Y., and J. D. Herring, 2012: Energy spectra of stably stratified turbulence. *J. Fluid Mech.*, **698**, 19–50, https://doi.org/10.1017/jfm.2011.546.

Klymak, J. M., and J. N. Moum, 2007: Oceanic isopycnal slope spectra. Part I: Internal waves. *J. Phys. Oceanogr.*, **37**, 1215–1231, https://doi.org/10.1175/JPO3073.1.

Kunze, E., E. Firing, J. M. Hummon, T. K. Chereskin, and A. M. Thurnherr, 2006: Global abyssal mixing inferred from lowered ADCP shear and CTD strain profiles. *J. Phys. Oceanogr.*, **36**, 1553–1576, https://doi.org/10.1175/JPO2926.1.

Latarius, K., U. Schauer, and A. Wisotzki, 2019: Near-ice hydrographic data from Seaglider missions in the western Greenland Sea in summer 2014 and 2015. *Earth Syst. Sci. Data*, **11**, 895–920, https://doi.org/10.5194/essd-11-895-2019.

Lindborg, E., 2006: The energy cascade in a strongly stratified fluid. *J. Fluid Mech.*, **550**, 207–242, https://doi.org/10.1017/S0022112005008128.

MacKinnon, J. A., and M. C. Gregg, 2003: Mixing on the late-summer New England shelf—Solibores, shear, and stratification. *J. Phys. Oceanogr.*, **33**, 1476–1492, https://doi.org/10.1175/1520-0485(2003)033<1476:MOTLNE>2.0.CO;2.

——, and Coauthors, 2009: Using global arrays to investigate internal-waves and mixing. *Proc. OceanObs'09 Conf.: Sustained Ocean Observations and Information for Society*, Venice, Italy, ESA, https://doi.org/10.5270/OceanObs09.cwp.58.

——, and Coauthors, 2017: Climate process team on internal wave–driven ocean mixing. *Bull. Amer. Meteor. Soc.*, **98**, 2429–2454, https://doi.org/10.1175/BAMS-D-16-0030.1.

Mater, B. D., S. K. Venayagamoorthy, L. St. Laurent, and J. N. Moum, 2015: Biases in Thorpe-scale estimates of turbulence dissipation. Part I: Assessments from large-scale overturns in oceanographic data. *J. Phys. Oceanogr.*, **45**, 2497–2521, https://doi.org/10.1175/JPO-D-14-0128.1.

Mauritzen, C., K. L. Polzin, M. S. McCartney, R. C. Millard, and D. E. West-Mack, 2002: Evidence in hydrography and density fine structure for enhanced vertical mixing over the Mid-Atlantic Ridge in the western Atlantic. *J. Geophys. Res.*, **107**, 3147, https://doi.org/10.1029/2001JC001114.

Merrifield, S. T., 2016: Mechanisms for enhanced turbulence in the Drake Passage region of the Southern Ocean. Ph.D. dissertation, Massachusetts Institute of Technology, 134 pp.

——, L. S. Laurent, B. Owens, A. M. Thurnherr, and J. M. Toole, 2016: Enhanced diapycnal diffusivity in intrusive regions of the Drake Passage. *J. Phys. Oceanogr.*, **46**, 1309–1321, https://doi.org/10.1175/JPO-D-15-0068.1.

Munk, W., 1981: Internal waves and small scale processes. *Evolution of Physical Oceanography*, B. Warren and C. Wunch, Eds., MIT Press, 264–291.

Nikurashin, M., and R. Ferrari, 2010: Radiation and dissipation of internal waves generated by geostrophic motions impinging on small-scale topography: Application to the Southern Ocean. *J. Phys. Oceanogr.*, **40**, 2025–2042, https://doi.org/10.1175/2010JPO4315.1.

——, ——, N. Grisouard, and K. Polzin, 2014: The impact of finite-amplitude bottom topography on internal wave generation in the Southern Ocean. *J. Phys. Oceanogr.*, **44**, 2938–2950, https://doi.org/10.1175/JPO-D-13-0201.1.

Polzin, K. L., and Y. V. Lvov, 2011: Toward regional characterizations of the oceanic internal wavefield. *Rev. Geophys.*, **49**, RG4003, https://doi.org/10.1029/2010RG000329.

——, J. M. Toole, and R. W. Schmitt, 1995: Finescale parameterizations of turbulent dissipation. *J. Phys. Oceanogr.*, **25**, 306–328, https://doi.org/10.1175/1520-0485(1995)025<0306:FPOTD>2.0.CO;2.

——, A. C. Naveira Garabato, T. N. Huussen, B. M. Sloyan, and S. Waterman, 2014: Finescale parameterizations of turbulent dissipation. *J. Geophys. Res. Oceans*, **119**, 1383–1419, https://doi.org/10.1002/2013JC008979.

Schmitt, R. W., 1994: Double diffusion in oceanography. *Annu. Rev. Fluid Mech.*, **26**, 255–285, https://doi.org/10.1146/annurev.fl.26.010194.001351.

Scotti, A., 2015: Biases in Thorpe-scale estimates of turbulence dissipation. Part II: Energetics arguments and turbulence simulations. *J. Phys. Oceanogr.*, **45**, 2522–2543, https://doi.org/10.1175/JPO-D-14-0092.1.

Sheen, K. L., and Coauthors, 2013: Rates and mechanisms of turbulent dissipation and mixing in the Southern Ocean: Results from the Diapycnal and Isopycnal Mixing Experiment in the Southern Ocean (DIMES). *J. Geophys. Res. Oceans*, **118**, 2774–2792, https://doi.org/10.1002/jgrc.20217.

——, J. A. Brearley, A. C. Naveira Garabato, D. A. Smeed, L. St. Laurent, M. P. Meredith, A. M. Thurnherr, and S. N. Waterman, 2015: Modification of turbulent dissipation rates by a deep Southern Ocean eddy. *Geophys. Res. Lett.*, **42**, 3450–3457, https://doi.org/10.1002/2015GL063216.

St. Laurent, L., and S. Merrifield, 2017: Measurements of near-surface turbulence and mixing from autonomous ocean gliders. *Oceanography*, **30** (2), 116–125, https://doi.org/10.5670/oceanog.2017.231.

——, A. C. Naveira Garabato, J. R. Ledwell, A. M. Thurnherr, J. M. Toole, and A. J. Watson, 2012: Turbulence and diapycnal mixing in Drake Passage. *J. Phys. Oceanogr.*, **42**, 2143–2152, https://doi.org/10.1175/JPO-D-12-027.1.

Talley, L. D., 2013: Closure of the global overturning circulation through the Indian, Pacific, and Southern Oceans: Schematics and transports. *Oceanography*, **26** (1), 80–97, https://doi.org/10.5670/oceanog.2013.07.

Tamsitt, V., and Coauthors, 2017: Spiraling pathways of global deep waters to the surface of the Southern Ocean. *Nat. Commun.*, **8**, 172, https://doi.org/10.1038/s41467-017-00197-0.

Thompson, A. F., 2008: The atmospheric ocean: Eddies and jets in the Antarctic Circumpolar Current. *Philos. Trans. Roy. Soc.*, **366A**, 4529–4541, https://doi.org/10.1098/rsta.2008.0196.

Thorpe, S. A., 1977: Turbulence and mixing in a Scottish loch. *Philos. Trans. Roy. Soc.*, **286A**, 125–181, https://doi.org/10.1098/rsta.1977.0112.

——, 2005: *The Turbulent Ocean.* Cambridge University Press, 439 pp.

——, 2012: Measuring overturns with gliders. *J. Mar. Res.*, **70**, 93–117, https://doi.org/10.1357/002224012800502417.

Waterhouse, A. F., and Coauthors, 2014: Global patterns of diapycnal mixing from measurements of the turbulent dissipation rate. *J. Phys. Oceanogr.*, **44**, 1854–1872, https://doi.org/10.1175/JPO-D-13-0104.1.

Waterman, S., A. C. Naveira Garabato, and K. L. Polzin, 2013: Internal waves and turbulence in the Antarctic Circumpolar Current. *J. Phys. Oceanogr.*, **43**, 259–282, https://doi.org/10.1175/JPO-D-11-0194.1.

Welch, P., 1967: The use of fast Fourier transform for the estimation of power spectra: A method based on time averaging over short, modified periodograms. *IEEE Trans. Audio Electroacoust.*, **15**, 70–73, https://doi.org/10.1109/TAU.1967.1161901.

Whalen, C. B., L. D. Talley, and J. A. MacKinnon, 2012: Spatial and temporal variability of global ocean mixing inferred from Argo profiles. *Geophys. Res. Lett.*, **39**, L18612, https://doi.org/10.1029/2012GL053196.

——, J. A. MacKinnon, L. D. Talley, and A. F. Waterhouse, 2015: Estimating the mean diapycnal mixing using a finescale strain parameterization. *J. Phys. Oceanogr.*, **45**, 1174–1188, https://doi.org/10.1175/JPO-D-14-0167.1.